Bioactive Materials 43 (2025) 82–97

Contents lists available at ScienceDirect

Bioactive Materials

journal homepage: www.keaipublishing.com/en/journals/bioactive-materials

Ultrasound-generated bubbles enhance osteogenic differentiation of mesenchymal stromal cells in composite collagen hydrogels

Somnath Maji [a], Mitra Aliabouzar [a,b], Carole Quesada [a], Anjali Chiravuri [a,c], Aidan Macpherson [a,c], Abigail Pinch [a,c], Karsyn Kazyak [a], Ziyad Emara [a], Bachir A. Abeid [b], Robert N. Kent III [c], Firaol S. Midekssa [c], Man Zhang [a], Brendon M. Baker [c,d], Renny T. Franceschi [c,e], Mario L. Fabiilli [a,c,f,*]

[a] Department of Radiology, University of Michigan, Ann Arbor, MI, USA
[b] Department of Mechanical Engineering, University of Michigan, Ann Arbor, MI, USA
[c] Department of Biomedical Engineering, University of Michigan, Ann Arbor, MI, USA
[d] Department of Chemical Engineering, University of Michigan, Ann Arbor, MI, USA
[e] Department of Periodontics and Oral Medicine, University of Michigan, Ann Arbor, MI, USA
[f] Applied Physics Program, University of Michigan, Ann Arbor, MI, USA

ARTICLE INFO

Keywords:
Ultrasound
Acoustic droplet vaporization
Collagen
Mesenchymal stromal cell
Differentiation
Mechanobiology
Biomaterial
Spatiotemporal

ABSTRACT

Hydrogels can improve the delivery of mesenchymal stromal cells (MSCs) by providing crucial biophysical cues that mimic the extracellular matrix. The differentiation of MSCs is dependent on biophysical cues like stiffness and viscoelasticity, yet conventional hydrogels cannot be dynamically altered after fabrication and implantation to actively direct differentiation. We developed a composite hydrogel, consisting of type I collagen and phase-shift emulsion, where osteogenic differentiation of MSCs can be non-invasively modulated using ultrasound. When exposed to ultrasound, the emulsion within the hydrogel was non-thermally vaporized into bubbles, which locally compacted and stiffened the collagen matrix surrounding each bubble. Bubble growth and matrix compaction were correlated, with collagen regions proximal (i.e., $\leq$ ~60 μm) to the bubble displaying a 2.5-fold increase in Young's modulus compared to distal regions (i.e., $>$ ~60 μm). The viability and proliferation of MSCs, which were encapsulated within the composite hydrogel, were not impacted by bubble formation. In vitro and in vivo studies revealed encapsulated MSCs exhibited significantly elevated levels of RUNX2 and osteocalcin, markers of osteogenic differentiation, in collagen regions proximal to the bubble compared to distal regions. Additionally, alkaline phosphatase activity and calcium deposition were enhanced adjacent to the bubble. An opposite trend was observed for CD90, a marker of MSC stemness. Following subcutaneous implantation, bubbles persisted in the hydrogels for two weeks, which led to localized collagen alignment and increases in nuclear asymmetry. These results are a significant step toward controlling the 3D differentiation of MSCs in a non-invasive and on-demand manner.

1. Introduction

Bone loss resulting from factors such as trauma [1] and diseases [2,3] represents a significant global challenge and remains a focal point of research [4,5]. A comprehensive study conducted in 2019 revealed that there were 178 million new fractures globally, with 455 million prevalent cases experiencing acute or chronic symptoms related to fractures [6]. While autologous and allogeneic bone transplants are commonly employed, they are constrained by restricted supply, prolonged recovery times, and donor site morbidity [7,8]. Recent advancements in tissue engineering and the utilization of mesenchymal stromal cells (MSCs), which are adult skeletal progenitor cells, have emerged as a significant area of interest in augmenting bone tissue reconstruction [9,10]. Despite promising preclinical results [11,12], MSC-based therapies have encountered translational hurdles. For instance, many clinically approved MSC-based products rely on local administration without

Peer review under responsibility of KeAi Communications Co., Ltd.
* Corresponding author. University of Michigan, 1301 Catherine Street, 6436C Medical Sciences Building I, Ann Arbor, MI, 48109, USA.
E-mail address: mfabiill@umich.edu (M.L. Fabiilli).

https://doi.org/10.1016/j.bioactmat.2024.09.018
Received 23 April 2024; Received in revised form 30 August 2024; Accepted 13 September 2024

accompanying carrier materials [13], which can result in inadequate retention and survival of MSCs at the site of administration [14]. Consequently, researchers are encapsulating MSCs within hydrogels that mimic the native extracellular matrix (ECM), thereby enhancing cell retention and viability [15].

MSCs sense and react to both biochemical and biophysical cues present within the ECM, which are intricately regulated in a spatial and temporal manner in response to physiological and pathological stimuli [16]. The differentiation of MSCs is influenced by biophysical factors such as substrate stiffness [17,18], viscoelasticity [19], and surface topography [20] of their local microenvironment. MSCs tend to differentiate towards adipogenic or osteogenic lineages when cultured on soft or stiff substrates, respectively [21,22]. For example, MSCs exhibited adipogenic and osteogenic phenotypes when encapsulated within alginate hydrogels with elastic moduli in the range of 2.5–5 kPa and 11–30 kPa, respectively [23]. Analogously, in transglutaminase-crosslinked gelatin hydrogels, osteogenic differentiation of encapsulated MSCs correlated with degree of crosslinking and stiffness across yield strengths of 1.6–61 kPa [24]. Similar findings were also observed in polyethylene glycol (PEG) hydrogels with compressive moduli ranging from 0.2 to 59 kPa [25]. However, unlike native ECM, conventional hydrogels typically possess mechanically uniform properties, which cannot be dynamically altered after fabrication and implantation. This lack of dynamic tunability in hydrogel properties hinders active guidance of MSC differentiation as well as gaining fundamental insight on how dynamic changes in matrix stiffness affect MSC differentiation in 3D.

Previous approaches for dynamically modulating hydrogel stiffness and cellular behavior have relied on stimuli such as ultraviolet light, pH, temperature, and magnetic fields [26,27]. For example, PEG-based hydrogels with photocrosslinkable groups were stiffened with ultraviolet light, leading to changes in nuclear tension of MSCs cultured in 2D [28]. Conversely, irradiation of PEG hydrogels with photodegradable groups caused an increase in MSC spreading [29]. Hydrogels consisting of a pH-sensitive, triblock copolymer exhibited a reversible 40-fold change in stiffness from pH 7 to 8, which impacted cytoskeletal structure [30]. MSCs, which were cultured on polyacrylamide hydrogels containing iron particles, exhibited changes in RUNX2 expression following modulation of gel stiffness using magnetic fields [31]. In most cases, these strategies rely on the use of synthetic polymers or derivatized, natural polymers (e.g., gelatin methacrylate). Additionally, many approaches do not afford deep tissue penetration (e.g., light), external control (e.g., pH), or tight focusing (e.g., magnetic field) of the stimulus.

Ultrasound is a highly desirable modality for non-invasive, therapeutic applications due to its precise temporal and spatial characteristics, alongside its ability to penetrate the body at clinically relevant scale [32]. We have developed a composite hydrogel, termed an acoustically responsive scaffold (ARS), that can be modulated using ultrasound [33]. An ARS integrates a phase-shift emulsion into a hydrogel matrix. The emulsion, which contains a perfluorocarbon (PFC) liquid, undergoes a phase-shift into bubbles when exposed to ultrasound above a threshold amplitude. This non-thermal, liquid-to-gas phase shift is termed acoustic droplet vaporization (ADV) [34] and is due to the tensile component of the ultrasound wave [35]. Our prior research with fibrin-based ARSs revealed that mechanical strain induced by an ADV-generated bubble on the surrounding matrix led to substantial, local compaction and stiffening of the matrix adjacent to the matrix–bubble interface [36,37]. This radial compaction of the hydrogel is due to the volumetric expansion of the PFC phase during ADV, followed by the growth of the ADV-generated bubble because of inward diffusion of gases from the local microenvironment. ADV-induced stiffening is observed in strain-stiffening matrices, such as natural biopolymers like fibrin. Given that stiffer substrates direct the differentiation of MSCs towards osteogenic lineages [21,38], we hypothesized that ADV could be used to dynamically and spatiotemporally control MSC differentiation.

In this study, we developed type I collagen-based ARSs. Collagen, the most abundant protein in the ECM that accounts for a significant fraction of connective tissues including bone, was selected due to its physiological relevance and osteoinductive properties [39]. Confocal microscopy was employed to quantify ADV-induced changes in the microstructure of ARSs, including dynamics of bubble growth and matrix compaction, while atomic force microscopy (AFM) was used to characterize micromechanical properties of ARSs before and after ADV. We encapsulated murine MSCs in ARSs for in vitro and in vivo investigations of osteogenic differentiation. Through confocal imaging, we observed an inverse correlation between the expression of bone markers such as RUNX2 and osteocalcin and the distance from an ADV-induced bubble. We also characterized alkaline phosphatase activity, calcium deposition, bubble morphology, and collagen structure of the ARSs. Overall, the data underscore the efficacy of ADV in dynamically modulating collagen compaction in ARSs and promoting osteogenic differentiation of MSCs.

2. Materials and methods

Cell Culture: Mouse bone marrow derived D1 MSC cells (CRL-12424, ATCC, Manassas, VA, USA) were cultured in growth medium containing high glucose Dulbecco's modified Eagle medium (DMEM, Gibco, Carlsbad, CA, USA) supplemented with 10% (v/v) fetal bovine serum (Corning, Glendale, AZ, USA), and 1% (v/v) penicillin/streptomycin in a humidified cell culture incubator with 5% CO_2 at 37 °C. The cells were grown to 70% confluency before subculturing. All experiments in this study were carried out with cell passage number 3 and 4.

Microfluidic preparation of phase-shift double emulsion (PSDE): PSDEs with a water-in-PFC-in-water (W_1/PFC/W_2) structure were produced by a microfluidic technique as previously described [36]. Perfluorohexane (C_6F_{14}, CAS# 355-42-0, Strem Chemicals, Newburyport, MA, USA) was the PFC phase. Fluorosurfactant copolymer, derived from a 2:1 M ratio of Krytox 157 FSH (CAS# 51798-33-5, DuPont, Wilmington, DE, USA) and poly(ethylene glycol)bis(amine) (MW: 1000 g mol^{-1}, CAS# 24991-53-5, Alfa Aesar, Ward Hill, MA, USA), was dissolved in PFC at 2% (w/w). This PFC solution was then combined at a 2:1 (v/v) ratio with a W_1 phase of phosphate-buffered saline (PBS, Corning), followed by 30 s of sonication on ice to produce the primary emulsion (W_1/PFC). PSDEs were generated by flowing the primary emulsion and W_2 phase (50 mg mL^{-1} Pluronic F68 in PBS) through a quartz microfluidic chip (Cat# 3200146, junction: 14 μm × 17 μm, Dolomite, Royston, United Kingdom) at 0.5 μL min^{-1} and 2.5 μL min^{-1}, respectively (Fig. 1A). Analysis using a Coulter Counter (Multisizer 4, Beckman Coulter, Brea, CA, USA) equipped with a 50 μm aperture tube revealed that the PSDEs had an average diameter, coefficient of variation, and concentration of 12.06 ± 0.79 μm, 6.82 ± 0.3%, and (5.18 ± 1.1) × 10^8 particles per mL, respectively.

Preparation of type I collagen-based ARSs: Type I collagen from rat tail (10 mg mL^{-1} in 0.02 M acetic acid, Advanced Biomatrix, Carlsbad, CA, USA) and neutralization solution (i.e., 10X DMEM, 1N NaOH, and 7.5% $NaHCO_3$) were degassed in a vacuum chamber at ~6 kPa for 30 min to reduce dissolved gas content. ARSs (volume = 0.2 mL) were created by combining the neutralization solution, collagen, and PSDE to yield ARSs with 6 mg mL^{-1} collagen and 0.05% (v/v) PSDE. For visualization of the collagen matrix, 50 μg mL^{-1} FITC-labeled, type I collagen (Sigma-Aldrich, St. Louis, MO, USA) was added to each ARS before polymerization in a custom plastic plate (well diameter: 9.5 mm, well height: 5.5 mm). The bottom and top of the well were sealed with a Tegaderm membrane (3M Healthcare, St. Paul, MN, USA). To prepare cell-loaded constructs, MSCs were trypsinized and mixed with the neutralized collagen solution at 10^6 cells mL^{-1}. Collagen-only gels (i.e., without PSDE) were prepared similarly. All gels were allowed to polymerize for 30 min at 37 °C before adding growth media. For differentiation studies, MSC-loaded constructs were cultured in bipotential differentiation media consisting of a 1:1 (v/v) mixture of osteogenic (A1007201, Gibco) and adipogenic (A1007001, Gibco) induction media, unless otherwise noted.

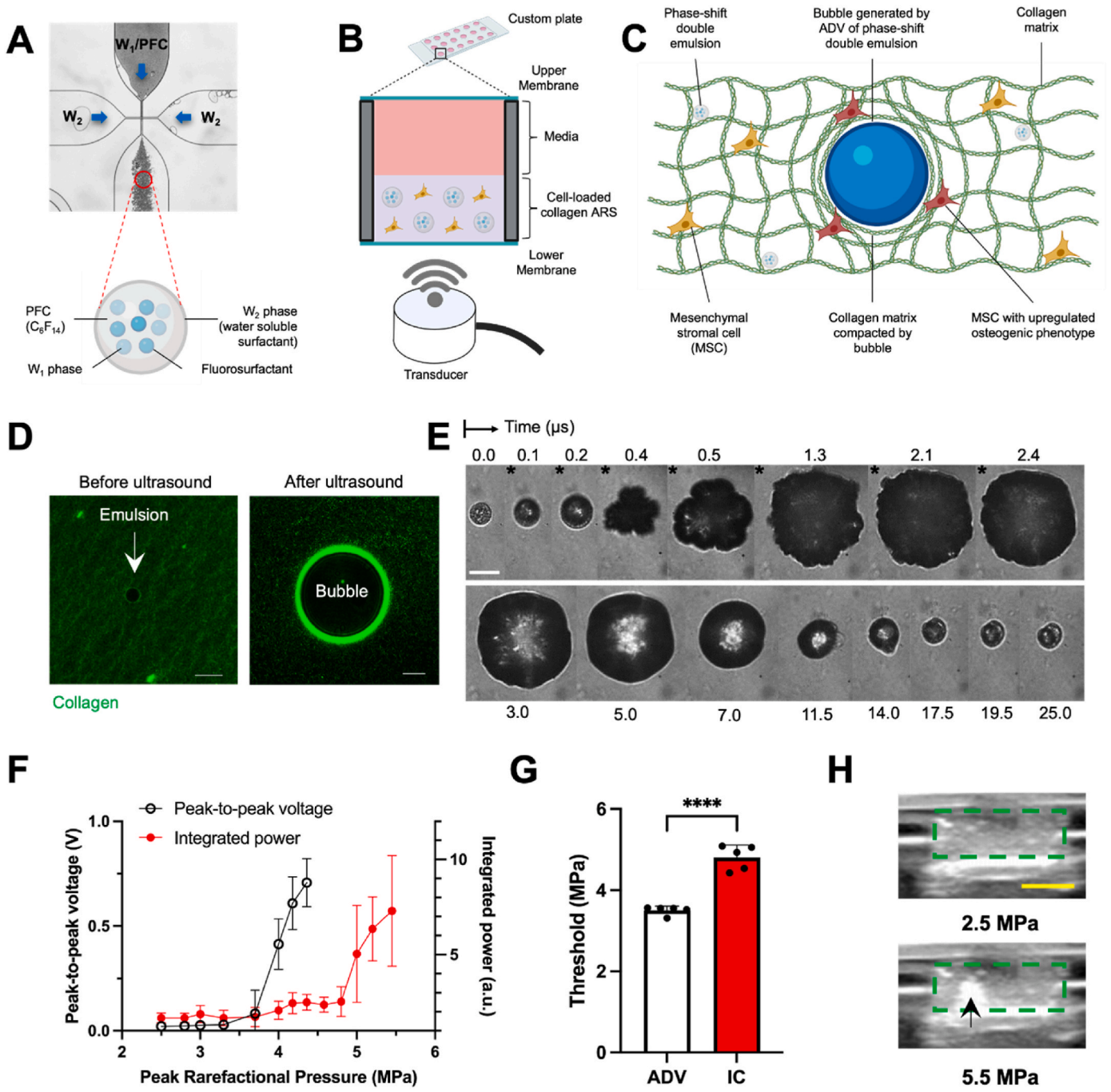

Fig. 1. Ultrasound generates bubbles in collagen ARSs. A) An image of the microfluidic chip shows the flow focusing geometry of the junction. The primary emulsion (W_1/PFC) was encapsulated by the W_2 phase to create a PSDE. The enlarged feature displays a schematic of a PSDE droplet. B) An ARS containing PSDE within a custom plate. For in vitro studies, the plate was submerged in a water tank and ultrasound was applied through the well bottom. C) During ADV, the PSDE is converted into a bubble, which locally compacts and stiffens the collagen matrix surrounding the bubble. D) Confocal microscopy images of an ARS before and 1 day after ultrasound exposure are shown. The elevated intensity of collagen surrounding the bubble is due to matrix compaction. Scale bar: 25 μm. E) Ultra-high-speed images show a PSDE droplet in a collagen hydrogel while being exposed to a single 2.4 μs burst of 2.5 MHz ultrasound at 4 MPa peak negative pressure. Presence of ultrasound in the field of view is denoted with an asterisk. Time stamps are listed next to each frame. Scale bar: 20 μm. F) Profiles of peak-to-peak voltage and broadband noise, which are indicative of ADV and IC, respectively, are shown for ARSs with 6 mg mL^{-1} collagen G) The IC threshold was significantly higher than the ADV threshold in collagen ARSs (N = 5). H) B-mode images highlight ADV-induced bubble formation (denoted by the black arrow) in collagen ARSs. The borders of the ARS are denoted by the green rectangle. Scale bar: 5 mm. Significant differences are denoted as follows: ****$p < 0.0001$.

Ultrasound exposure setup and parameters: Ultrasound experiments were conducted in a tank (32 cm × 61 cm × 32 cm) filled with degassed, deionized water at 37 °C. ADV was induced using a calibrated, focused transducer (2.5 MHz, H-108, f-number: 0.83, radius of curvature: 50 mm, Sonic Concepts, Bothell, WA, USA). Pulsed waveforms (pulse duration: 6 μs; pulse repetition frequency: 100 Hz) were generated by a function generator (33500B, Agilent Technologies, Santa Clara, CA, USA) and amplified by a gated radiofrequency (RF) amplifier (GA-2500A, Ritec, Warwick, RI, USA). The amplified signals were monitored in real-time on an oscilloscope (HDO4034, Teledyne LeCroy, Chestnut Ridge, NY, USA).

In vitro experiments were performed by submerging the custom plate

containing the ARSs in the water tank (Fig. 1B). The transducer, which was placed beneath the plate, was connected to a three-axis positioning system controlled by MATLAB (The MathWorks, Natick, MA, USA). To generate ADV, the transducer was rastered at 5 mm s^{-1} with 0.5 mm spacing between raster lines. The transducer was rastered on three planes by placing the axial focus 1, 2, and 3 mm above the well bottom. Exposures were completed from +3 mm to +1 mm.

Determination of acoustic thresholds: Acoustic thresholds in collagen ARSs were determined following established protocols [40–42]. ARSs were exposed to pulsed ultrasound of increasing acoustic pressure while a capsule hydrophone (HGL-1000, frequency range 1–20 MHz, Onda, Sunnyvale, CA, USA) captured backscattered signals. Concurrently, a diagnostic ultrasound imaging system (ZS3, Mindray North America, Mountain View, CA, USA) with a 12 MHz linear array (L14-5w, Mindray) recorded B-mode images of bubble formation. The radiofrequency signals collected by the hydrophone were digitized by an oscilloscope and analyzed using MATLAB. The ADV and inertial cavitation (IC) thresholds were determined by plotting the peak-to-peak amplitude and integrated frequency power spectrum of the scattered response, respectively, as a function of peak rarefactional pressure. Thresholds were defined as the intersection of two linear fits for each profile. B-mode images were analyzed in Fiji (National Institutes of Health, Bethesda, MD, USA) by calculating the average pixel intensity within a defined region of interest in the ARS.

Ultra-high-speed dynamics of bubble growth: Bubble dynamics were visualized with ultra-high-speed imaging using a previously published method [43]. The ARS was mounted on the stage of a confocal microscope (AX, Nikon, Tokyo, Japan). ADV was generated using a single pulse of 2.5 MHz ultrasound emitted by a focused transducer coupled to the ARS with a water-filled cone. The optical focus of the microscope objective and acoustic focus of the transducer were confocally aligned. An ultra-high-speed camera (HPV-X2, Shimadzu, Kyoto, Japan), which was connected to the microscope, enabled acquisition of 256 frames at up to 10 million frames per second. Illumination was provided by a high intensity pulsed laser (400 W, 640 nm, Cavitar, Tampere, Finland).

Optical and micromechanical characterization of acellular ARSs: To investigate ADV-induced microstructural changes (Fig. 1C), acellular ARSs were imaged from 1 h to 7 days after ADV using confocal microscopy. Laser power was set to the lowest non-zero setting to prevent saturation of the FITC-collagen signal. Bubble diameter and the width of the collagen matrix compacted by the bubble were measured in NIS-Elements (Nikon). The latter parameter was defined as the maximum distance from the bubble-collagen interface that displayed an intensity of FITC-collagen at least two-fold higher than the bulk collagen gel.

To quantify bubble-induced matrix stiffening, acellular collagen ARSs (height: ~1 mm) were immobilized on poly-L-lysine coated coverslips. Force–indentation curves were acquired on collagen-only gels and ARSs using an AFM (FlexAFM, Nanosurf, Liestal, Switzerland) mounted on an inverted, epifluorescent microscope (Eclipse Ti, Nikon). A gold-coated AFM probe (PPP-CONTAuD, NanoAndMore, Watsonville, CA, USA) was used to mechanically interrogate the samples in contact mode. Before measurements, the cantilever's spring constant was determined automatically using the built-in thermal tuning method. The compressive Young's modulus was estimated from the force–indentation curves using the DMT model in AtomicJ software (http://sourceforge.net/projects/jrobust) [36].

Cellular metabolic activity and viability assays: To assess the viability of encapsulated MSCs, constructs were stained with 500 nM propidium iodide (PI, Invitrogen, Waltham, MA, USA) in DMEM for 10 min, followed by counterstaining with Hoechst 33342 (Invitrogen). Constructs were then imaged with confocal microscopy. Using a custom script (NIS Elements), the number of PI^+ cells was calculated as a function of distance from the bubble-collagen interface.

Metabolic activity of the constructs was assessed using the alamar blue assay (Invitrogen) as done previously [44]. Constructs were incubated in 10% (v/v) alamar blue reagent in DMEM for 4 h. After incubation, absorbances of the supernatants were measured at 570 nm and 600 nm using a plate reader (SpectraMax M2e, Molecular Devices, San Jose, CA, USA), and analyzed according to the manufacturer's instructions.

Differentiation assays: Alkaline phosphatase (ALP) activity of constructs was assessed after 7 and 14 days of incubation in bipotential media. Constructs were digested with a collagenase solution (2 mg mL^{-1}) and cells were concentrated via centrifugation at 14,000g for 15 min. The cell-containing mixture was combined with RIPA buffer (Thermo Scientific), incubated on ice for 30 min, and centrifuged for 15 min at 14,000g. ALP activity of the supernatant, which contained soluble proteins, was measured using a commercially available kit (EEA002, Invitrogen) by detecting absorbance at 520 nm. ALP activity (i.e., King unit/g protein) was calculated as per the manufacturer's instructions and normalized by the total protein concentration, which was measured using the BCA assay.

Constructs were also cultured for 14 days in growth media supplemented with 100 nM dexamethasone, 250 μM L-ascorbic acid, and 10 mM β-glycerophosphate. Calcium deposition was assessed by Alizarin Red S (#A5533, Sigma-Aldrich; pH 4.2) staining.

In vivo studies: All animal procedures were approved by the University of Michigan Institutional Animal Care and Use Committee. Male BALB/c nude mice (N = 14, 6–8 weeks old, 19.3 ± 2.3 g, Charles River Laboratories, Wilmington, MA, USA) were utilized as hosts. Mice were anesthetized with isoflurane and the dorsal skin was scrubbed with povidone-iodine. Two full-thickness longitudinal incisions were made in the lower dorsal region on either side of the spine, creating subcutaneous pockets. Cell-loaded constructs were implanted into the pockets, and the surgical sites were closed with sutures. The next day, subsets of constructs were treated with 2.5 MHz ultrasound (4.2 MPa peak negative pressure, pulse duration: 6 μs; pulse repetition frequency: 100 Hz, raster speed: 5 mm s^{-1}). During treatment, each mouse was anesthetized with isoflurane and placed in a supine position on an exposure platform positioned on the water tank. Construct morphology was monitored using B-mode ultrasound imaging with a 24 MHz linear array (L30-8, Mindray). Construct height and average pixel intensity were measured in Fiji. The implanted constructs and surrounding tissue were harvested on day 7 or 14 post implantation.

Cell staining and analyses: Constructs were fixed in neutral buffered formalin. In vitro constructs were permeabilized with 0.1% (v/v) Triton X-100 and incubated overnight with primary antibodies against RUNX2 (ab192256, Abcam, Cambridge, United Kingdom), osteocalcin (23418-1-AP, Proteintech, Rosemont, IL, USA), CD90 (ab3105, Abcam), and PPAR-γ (ab45036, Abcam). An Alexa Fluor 647-labeled secondary antibody (ab150067, Abcam) was used for visualization in addition to Hoescht 33342 for counterstaining nuclei. In vivo samples were embedded in paraffin, sectioned, and mounted onto glass slides by the University of Michigan Orthopaedic Research Laboratories Histology Core. Slides were stained using the above antibodies. All samples were imaged with a confocal microscope. Marker expression was evaluated using a custom script (NIS Elements) that calculated the average fluorescent intensities in the nucleus and cytoplasm (i.e., perinuclear region) for each cell. Nuclear localization was obtained by dividing the average intensity in the nucleus by the average intensity in the cytoplasm. Marker expression for each cell, as well as nuclear circularity, was calculated as a function of distance from the nearest bubble edge.

Histological slides were stained with hematoxylin and eosin (H&E). Construct height and area as well as the number and diameter of bubbles were measured in Fiji. To assess the fibrillar collagen content and fiber alignment, slides were stained with picrosirius red (Fisher Scientific) per the manufacturer's instructions. Brightfield and polarized light images of the stained slides were captured using an upright microscope (Axioplan 2, Zeiss, Oberkochen, Germany). To quantify collagen content, Fiji was utilized to delineate the region of interest around the bubbles in each image and quantify red intensity as the ratio of red to the sum of red, green, and blue intensity for each pixel. A rotating stage then

facilitated image acquisition from −45° to 45° of deviation at 5° intervals, where deviation indicates the orientation along the long axis of the bubble-gel interface relative to the polarizer. A deviation of 0° was defined as the orientation displaying the brightest birefringence. Each field of view obtained was mutually exclusive. MATLAB was employed to calculate the birefringence intensity (i.e., average luminance) within a circular region of interest (50 μm radius) at the center of each polarized light image. To assess calcium deposition, paraffin-embedded sections of in vitro and in vivo constructs were stained with Alizarin Red S. To quantify mineralization, brightfield images were analyzed in Fiji software by defining a region of interest around the bubbles and quantifying the red intensity as the ratio of red to the sum of red, green, and blue intensity for each pixel. In vivo constructs were also immunohistochemically stained for CD31 (ab182981, Abcam) using a polymer-horseradish peroxidase conjugate (Envision + System-HRP (DAB), Agilent) and counterstained with hematoxylin. The density of blood vessels, defined as $CD31^+$ structures with a lumen, within the construct as well as the penetration depth of vessels into the construct were determined from brightfield images.

Statistical analysis: For experiments comparing only two groups, we used two-tailed, unpaired Student's t-tests. For experiments comparing multiple groups, we used one-way ANOVA and Tukey's multiple comparisons test. Unless otherwise noted, data are presented as mean ± standard deviation or as violin plots in which the first quartile, median, and third quartile are denoted.

3. Results

3.1. ADV radially compacts the hydrogel matrix in a collagen ARS

Before ultrasound exposure, the collagen matrix surrounding the PSDE appeared green due to the presence of FITC-collagen (Fig. 1D). Collagen-only gels, without PSDE, displayed a similar homogeneous distribution of FITC-collagen (not shown). Ultrasound exposure caused bubble formation and compaction of collagen fibers at the bubble-collagen interface, thereby locally elevating the fluorescence signal within the matrix. Fig. 1E shows sequential, ultra-high-speed images of a PSDE droplet undergoing ADV in a collagen ARS. The phase change was induced within 0.2 μs following the arrival of ultrasound, as seen in the change in refractive index of the liquid droplet into a bubble. The bubble contracted after the ultrasound pulse ceased and later grew. Spatiotemporally resolved ADV bubble dynamics are presented in Supplementary Video V1. The volumetric expansion of the PFC phase during ADV, followed by successive expansion and contraction cycles, induced repetitive localized strain to the gel, resulting in local microstructural rearrangement of the fibrillar, collagen network.

3.2. ADV and IC thresholds in collagen ARSs

The peak-to-peak voltage and integrated frequency power spectrum from ARSs at an excitation frequency of 2.5 MHz are depicted in Fig. 1F.

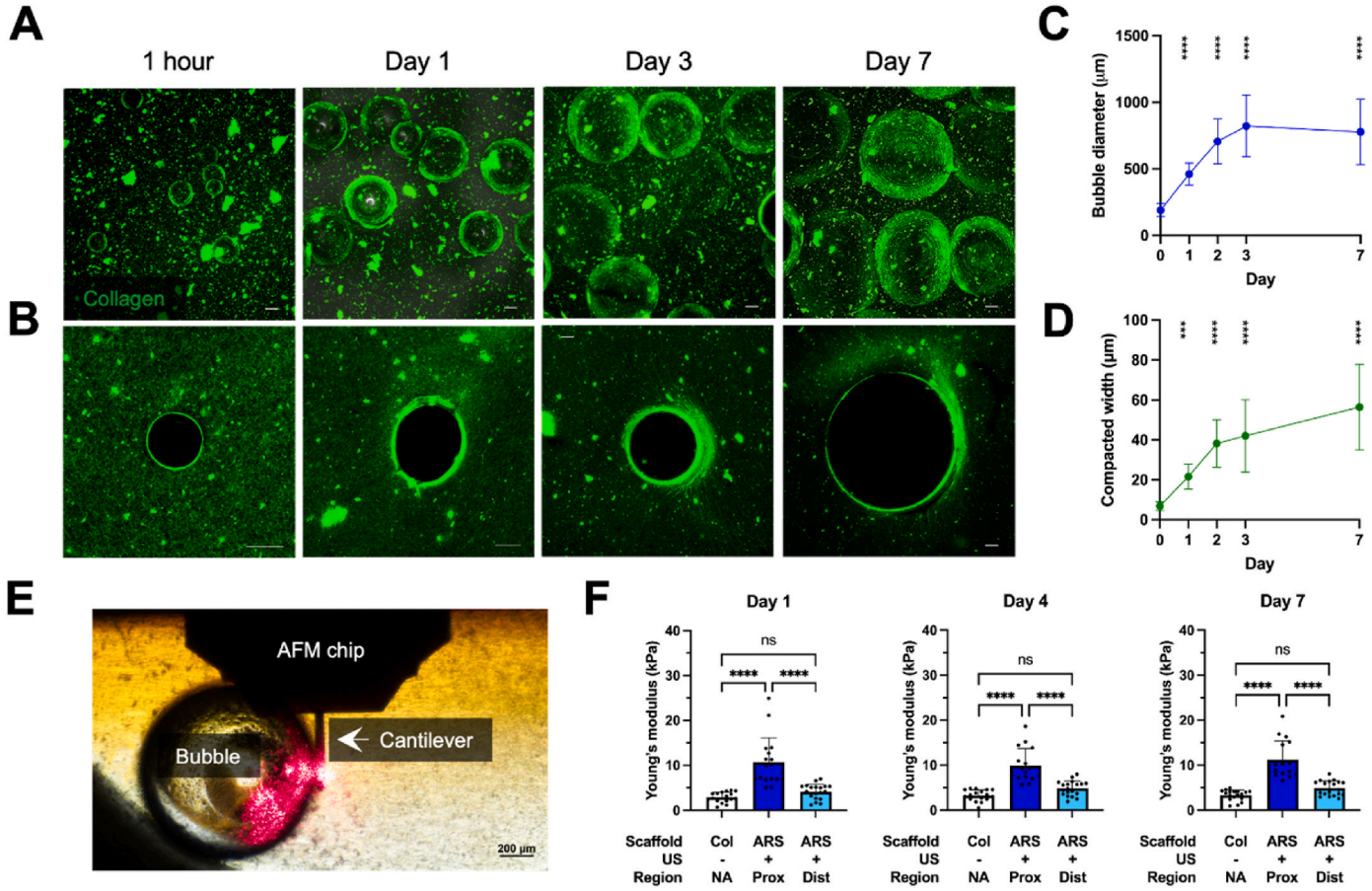

Fig. 2. Bubble growth and collagen compaction are linked. A) Maximum intensity projection of confocal images of ARSs at 1 h, 1 day, 3 days, and 7 days post-ADV (B) The confocal micrographs (i.e., single z-plane) show changes in collagen compaction around the ADV-generated bubble after 1 h, 1 day, 3 days, and 7 days. Scale bar = 100 μm. C) Bubble diameter and D) width of the compacted matrix region were measured following generation of ADV on day 0 (N = 14–28). (E) AFM was used to investigate time-dependent, micromechanical properties of ARSs post ADV. An optical image of an ARS 1 day post ADV shows the cantilever and bubble. (F) Calculated Young's moduli of a collagen-only gel (Col) as well as compacted, proximal (prox) and uncompacted, distal (dist) matrix regions of ARSs following exposure to suprathreshold ultrasound (US) (N = 16–19). Significant differences are denoted as follows: ***p < 0.001 and ****p < 0.0001; ns denotes a non-significant difference. In panels C and D, comparisons are relative to day 0.

Piecewise, linear fitting yielded ADV and IC thresholds of 3.5 ± 0.1 MPa and 4.8 ± 0.3 MPa, respectively (Fig. 1G). Across the interrogated pressures, control collagen-only gels exhibited no ADV, due to the absence of encapsulated PDSE, or IC thresholds (data not shown). B-mode images highlight the formation of a bubble cloud within an ARS (Fig. 1H). The ADV threshold obtained using B-mode imaging (data not shown) was not significantly different than the threshold measured using the hydrophone (Fig. 1F–G). A peak negative pressure of 4.2 MPa, which was suprathreshold for ADV and subthreshold for IC, was selected for all subsequent studies.

3.3. Optical and micromechanical characterization of collagen ARS

ADV-generated bubbles were longitudinally monitored using

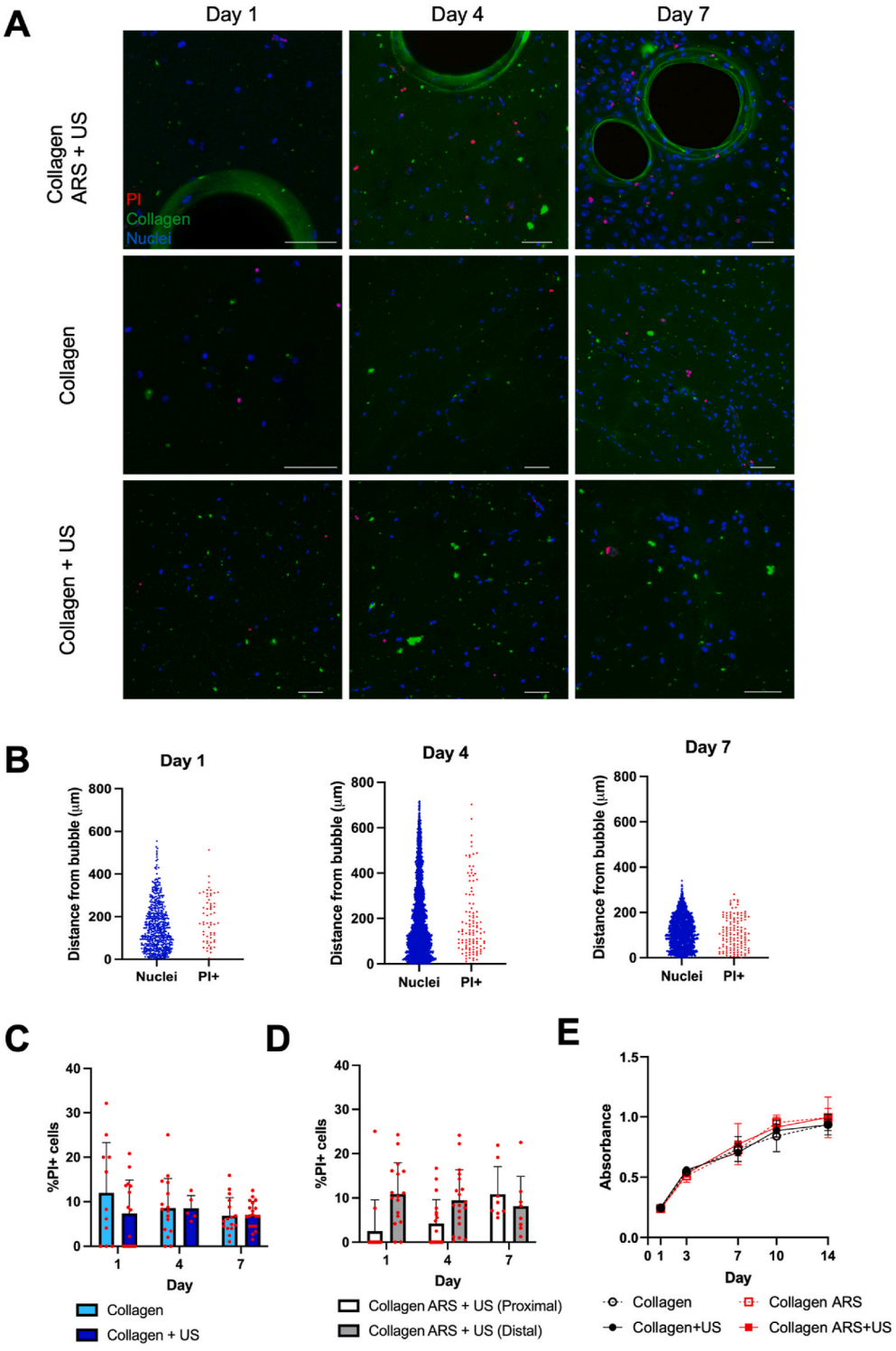

Fig. 3. ADV and bubble growth did not significantly impact cell viability and proliferation in ARSs. (A) Viability of encapsulated MSCs was investigated on day 1, day 4 and day 7 after ADV using PI-staining. Fluorescent images show cell-loaded ARSs and collagen-only gels. Scale bar = 100 μm. B) The spatial distribution of PI^+ cells from the collagen-bubble interface is displayed (N = 500–2500 cells per group). The percent of PI^+ cells is shown for C) collagen-only gels and D) ARSs. (N = 10–20 fields of view per group) (E) Cell proliferation was measured using the alamar blue assay (N = 4).

confocal microscopy. Fig. 2A and B displays maximum intensity projections and single z-planes, respectively, of ARSs at 1 h, 1 day, 3 days, and 7 days post-ADV. Qualitatively, the bubbles grew due to the influx of dissolved gases from the medium. The average bubble diameters were 189 ± 49 μm (1 h), 461 ± 83 μm (1 day), 706 ± 172 μm (2 days), 821 ± 232 μm (3 days), and 776 ± 245 μm (7 days) (Fig. 2C). The average bubble diameter grew 258 μm per day during the first two days and 115 μm per day from day 2 to day 3. Between day 3 and day 7, bubble size remained relatively constant.

The width of the compacted region of collagen around the ADV-generated bubble was quantified (Fig. 2D). The average width was 6.8 ± 2.2 μm on day 0 and increased to 56.5 ± 21.4 μm on day 7. The average increase in the width of the compacted region around the ADV-generated bubble was ~15 μm per day in the first two days, with a reduction to ~10 μm/day from day 3 onwards. Thus, bubble growth post ADV and matrix compaction were correlated, with both parameters leveling off by day 7. Based on these results, we used the average width of matrix compaction on day 7 (W_c) as the threshold between proximal and distal regions. For all subsequent experiments, a distance less than or equal to W_c from the bubble-collagen interface was defined as the compacted (i.e., proximal) collagen region whereas a distance greater than W_c was the uncompacted (i.e., distal) collagen region.

The AFM study revealed the micromechanical heterogeneity of ARSs post ADV, on the scale of the probe size (Fig. 2E and F). The Young's moduli of the matrix region proximal to the bubble were 10.7 ± 5.5 kPa (day 1), 9.9 ± 3.8 kPa (day 4), and 11.2 ± 4.2 kPa (day 7). Similarly, for the distal region, Young's moduli were 4.2 ± 1.7 kPa (day 1), 4.8 ± 1.7 kPa (day 4) and, 4.9 ± 1.6 kPa (day 7). By comparison, the Young's moduli for a collagen-only gel were 2.9 ± 1.1 kPa one day after polymerization and without any significant change on day 4 (3.3 ± 1.2 kPa) and day 7 (3.3 ± 1.2 kPa). Greater variation in Young's modulus in the bubble region of the ARSs stems from the difference in distances of the ADV-generated bubbles from the gel surface. Due to objective magnification and working distance restrictions, it was not possible to evaluate the depth of the bubbles.

3.4. Effect of ADV on MSC viability and proliferation

To visualize the effect of ADV on encapsulated MSCs, cell-loaded constructs were stained with PI, which penetrates cells with compromised membranes. Fig. 3A shows PI-staining in ARSs with ultrasound exposure as well as collagen-only gels with and without ultrasound exposure. The spatial distribution of all cells, along with PI^+ cells, relative to the bubble-collagen interface is also displayed (Fig. 3B). The percent of PI^+ cells is also shown for collagen-only gels (Fig. 3C) and ARSs (Fig. 3D). There were no significant differences when comparing across different groups or different time points. Thus, ADV and subsequent bubble growth did not significantly impact cell viability.

Proliferation of MSCs in the ARSs was assessed using the alamar blue assay (Fig. 3E). In this assay, resazurin is reduced by viable cells to resorufin, indirectly reflecting their metabolic activity and proliferation. The data exhibit a positive trend, indicating an increase in resazurin reduction over the 14-day study. At each time point, there were no significant differences between any of the groups. Thus, ADV and bubble growth did not impact the proliferative capacity of MSCs in ARSs.

3.5. ADV-induced matrix stiffening enhances osteogenic differentiation

Immunofluorescence staining was used to assess the impact of ADV-induced matrix stiffening on the differentiation of encapsulated MSCs cultured in bipotential differentiation media. The localization and expression levels of RUNX2 and osteocalcin (OCN), respectively, were assessed to evaluate the differentiation of MSCs towards an osteogenic lineage, while the expression of CD90 was utilized as a positive marker for MSC stemness. Fig. 4 presents confocal micrographs depicting the expression of these markers within the ARSs on day 7 and day 14. ADV was generated on day 0. Supplemental Fig. S1 shows images of collagen gels with and without ultrasound exposure.

RUNX2, a transcription factor, is a key regulator of osteoblast differentiation crucial for skeletal development and osteogenesis [45,46]. The nucleus-to-cytoplasm (N/C) ratio of RUNX2 was analyzed as a marker for osteogenic differentiation. Following ADV, MSCs located proximal to the bubble exhibited significantly greater levels of nuclear localization of RUNX2 compared to distal MSCs on both day 7 and day 14 (Fig. 4A–C). The mean N/C ratio of RUNX2 on day 7 in the proximal region (3.1 ± 1.4) was 24% higher than in the distal region (2.5 ± 1.4). This notable difference in N/C ratio of RUNX2 on day 7 indicates that cells near the bubble, experiencing a stiffened matrix, demonstrate more robust osteogenic differentiation than those farther away. A significant decrease in nuclear localization of RUNX2 was observed on day 14. Furthermore, the difference in the N/C ratio of proximal (2.3 ± 0.8) and distal (2.1 ± 0.9) regions was less on day 14 in both regions. The localization study of RUNX2 in collagen-only gels is shown for comparison (Fig. 4D). The percent difference between different groups and p-values for pairwise comparisons are found in Supplemental Fig. S2.

OCN serves as a middle-to-late-stage marker of osteoblast differentiation and is involved in initiating bone matrix mineralization [47]. On day 7, there was no significant difference in OCN expression between proximal and distal regions of the ARS (Fig. 4E–G), which is consistent with previous research indicating a low or undetectable expression of OCN during initial stages of differentiation [48]. OCN expression increased from day 7 to day 14. On day 14, MSCs in the proximal region exhibited significantly higher levels of OCN than in the distal region. The second week of in vitro osteogenic differentiation often marks a transition point where osteoblasts become more mature and actively produce mineralized matrix [49]. OCN expression at this stage reflects the maturation of osteoblasts and their ability to contribute to bone formation. OCN expression in collagen-only gels is shown for comparison (Fig. 4H).

We also investigated the expression of CD90 in ARSs on day 7 and day 14 (Fig. 4I–K). CD90 is a cell surface glycoprotein indicative of stemness-associated traits, such as self-renewal capacity and multipotent differentiation potential of MSCs [50]. There was higher expression of CD90 in the distal region of the ARS compared to the proximal region on both time points. This data indirectly suggests that the cells lost their characteristic stemness more readily when located closer to the bubble. CD90 expression in collagen-only gels is shown for comparison (Fig. 4L). CD90 expression in collagen-only gels was significantly higher compared to the ARSs (Supplemental Fig. S2).

ALP is an early-to-middle stage marker during osteogenic differentiation and plays a crucial role in the mineralization process of bone formation. Fig. 5C shows a significant increase in ALP activity in ultrasound-treated ARSs compared to untreated ARSs and collagen-only gels. For example, the mean ALP activity on day 14 for ultrasound-treated ARSs was 71% higher than untreated ARSs. There were no significant differences between collagen-only gels and untreated ARSs, indicating that unvaporized PSDE did not impact ALP activity.

Calcium deposition serves as a middle-to-late stage marker for osteoblast differentiation and indicates matrix mineralization. Elevated Alizarin red staining was observed proximal to bubbles in ARSs (Fig. 5A–B), indicating calcification within the construct. In contrast, minimal staining was seen in collagen-only constructs.

3.6. In vivo morphology of ARSs

Subcutaneously implanted, MSC-loaded constructs were monitored using B-mode ultrasound imaging (Fig. 6A). On day 0 (i.e., day of implantation), ARSs appeared significantly brighter (i.e., more echogenic) than collagen-only gels due to the PDSE (Fig. 6B). Following ADV on day 1, the echogenicity of ARSs increased due to bubble formation, which caused acoustic shadowing in some regions. The heights of the implanted constructs, determined from B-mode images, decreased over

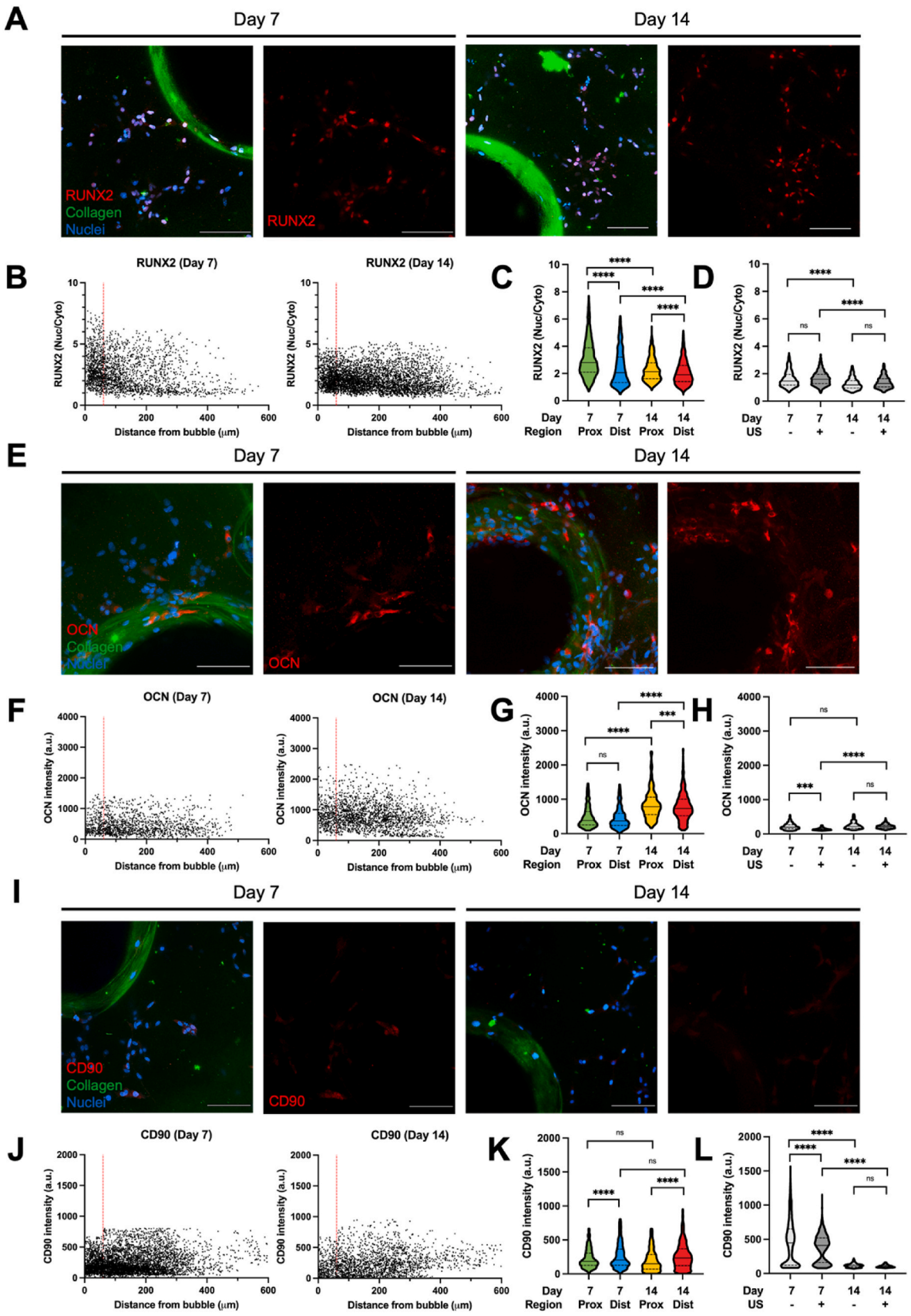

(caption on next page)

Fig. 4. Immunofluorescence was used to investigate the in vitro differentiation of MSCs in collagen ARSs. A) Confocal micrographs show the nuclear localization of RUNX2 in MSCs on day 7 and day 14. B) The N/C ratio of RUNX2 is plotted versus distance from the bubble-collagen interface. The dotted red line is W_c. The N/C ratio in C) ARSs and D) collagen-only gels with and without ultrasound (US) exposure on day 7 and day 14 is displayed. Proximal (prox) and distal (dist) regions are shown in panel C. N = 600–3800 cells per group. E) Confocal micrographs show the expression of OCN in MSCs on day 7 and day 14. F) The intensity of OCN expression is plotted versus distance from the bubble-collagen interface. OCN intensity in G) ARSs and H) collagen-only gels with and without US. N = 500–1800 cells per group. I) Confocal micrographs show the expression of CD90 in MSCs on day 7 and day 14. J) The intensity of CD90 expression is plotted versus distance from the bubble-collagen interface. CD90 intensity in K) ARSs and collagen-only gels with and without US. N = 400–4000 cells per group. Significant differences are denoted as follows: ***p < 0.001 and ****p < 0.0001; ns denotes a non-significant difference. All scale bars are 100 μm.

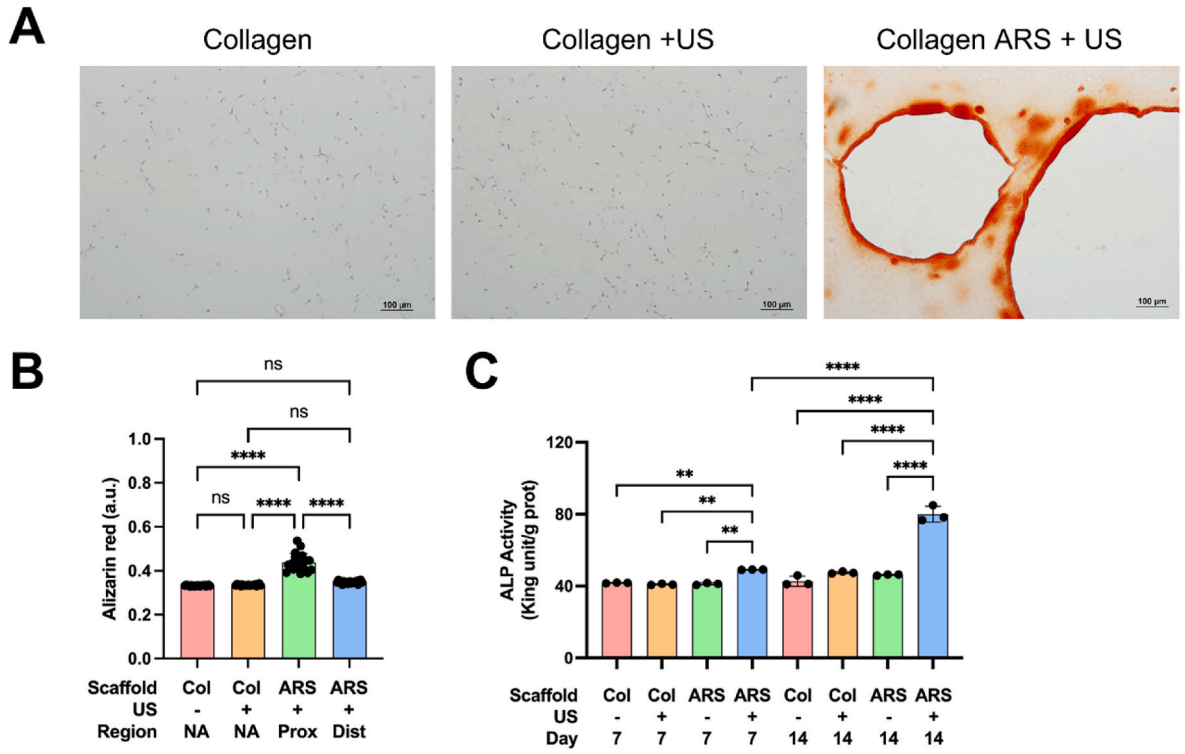

Fig. 5. Calcium deposition and ALP activity increased in vitro due to ADV-generated bubbles. A) After 14 days of culture, Alizarin red staining was enhanced in regions proximal to the bubbles. All scale bars are 100 μm. B) The intensity of Alizarin red staining was calculated for each construct. N = 3 constructs per group with 6-7 fields of view per constuct. C) ALP activity was significantly higher in ARSs exposed to ultrasound compared to other groups. Significant differences are denoted as follows: **p < 0.01 and ****p < 0.0001; ns denotes a non-significant difference. N = 3 constructs per group.

time (Fig. 6C). By day 3, collagen-only constructs were significantly smaller than ARSs. Thus, bubbles appear to mitigate ARS compaction. Due to acoustic shadowing, we were unable to calculate the height of ARSs at later time points (i.e., day 7, 10, and 14).

H&E-stained micrographs reveal the presence of numerous bubbles distributed throughout ARSs as well as cells in both ARSs and collagen-only constructs (Fig. 6D). Qualitatively, a higher number of cells was observed on day 14 compared to day 7, indicating ongoing cell proliferation after implantation. Construct height was measured from H&E images (Fig. 6E). The heights of collagen-only constructs were smaller than the ARS, though the difference was not statistically significant. This trend was consistent with our B-mode imaging data. Thus, ADV-generated based bubbles dampen construct compaction due to encapsulated cells and compressive forces exerted by the skin.

We also calculated bubble diameter (Fig. 6F), density (Fig. 6G), and area fraction (Fig. 6H) from H&E-stained slides. The average bubble diameter was significantly greater on day 14 (172 ± 88 μm) versus day 7 (144 ± 77 μm). The percent of bubbles with diameters 100 μm or smaller decreased from 41% on day 7–24% on day 14. The density of bubbles in the ARS decreased from day 7 to day 14, which was largely attributed to a 51% decrease in the number of bubbles. There was also a decrease in the area fraction occupied by bubbles.

3.7. ADV-induced matrix stiffening induced topographical alignment of collagen fibers and changes in nuclear morphology

The orientation and alignment of collagen fibers are crucial factors in bone healing, as they promote cell adhesion, migration, proliferation, and differentiation [51]. We stained histological slides with picrosirius red (Fig. 7), which enabled assessment of collagen content as well as maturity and alignment via quantification of birefringence when imaged under polarized light [52]. Fig. 7A displays picrosirius red-stained sections from day 7 and day 14. Intensity measurements reveal a significantly higher collagen concentration in the proximal region of the ARS compared to the distal region and collagen-only constructs (Fig. 7A–B). Birefringence imaging also indicated greater alignment of the collagen fibers in the proximal region of the ARS compared to the distal region and collagen-only constructs (Fig. 7C–F, Supplemental Fig. S3).

We also investigated how aligned topographical features impacted nuclear morphology within in vivo constructs (Supplemental Fig. S4). A circularity value of one indicates a perfect circle while values approaching zero reflect a highly elongated shape. On both day 7 and day 14, nuclear circularity was lower in the proximal region of the ARS compared to the distal region. In the proximal region, nuclei aligned with their long axes tangential to the bubble perimeter, indicating a strong dependency of cell morphology on local matrix alignment. Nuclear circularity was also higher in the collagen-only constructs.

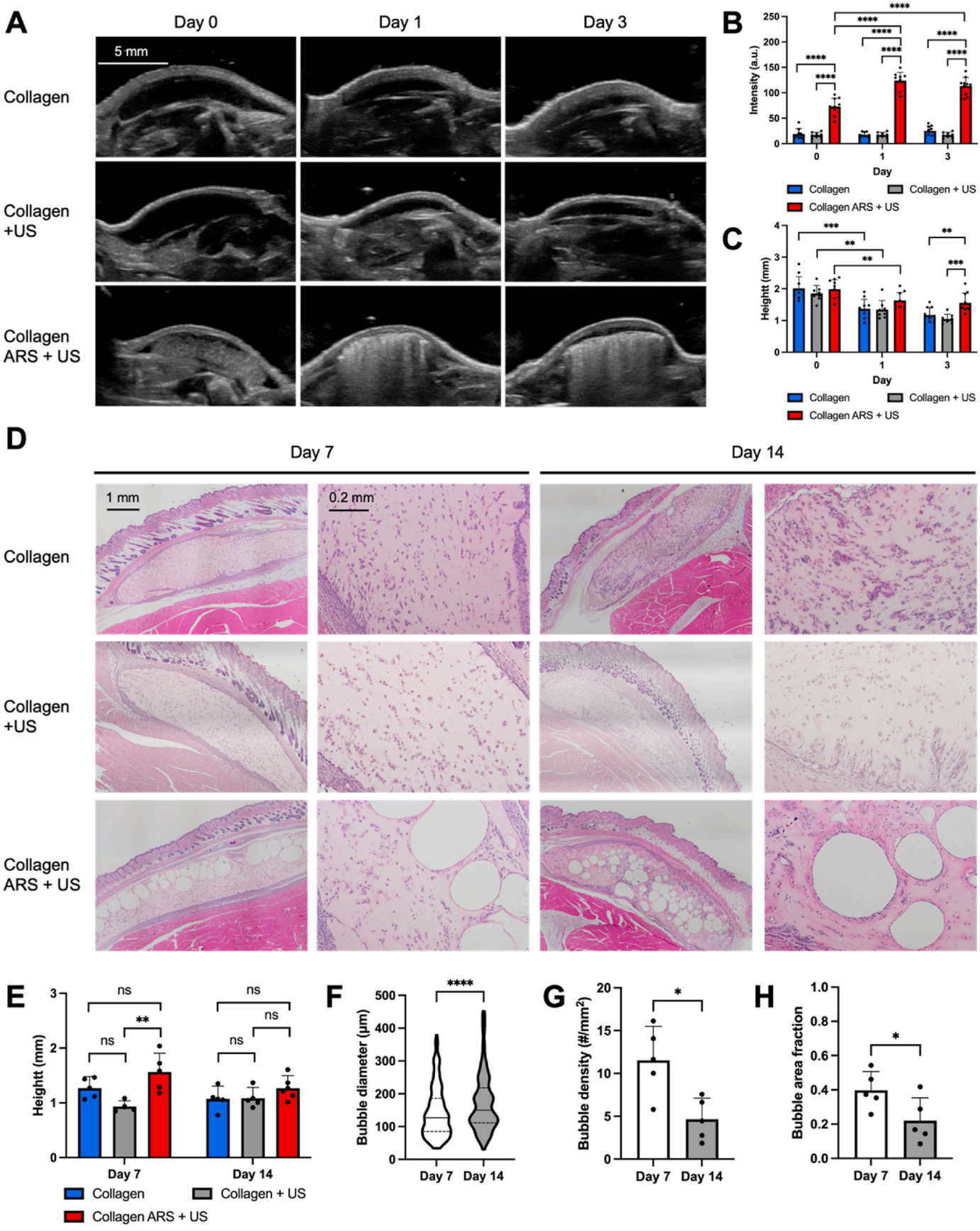

(caption on next page)

Fig. 6. ADV-generated bubbles impact ARS morphology. A) B-mode ultrasound images show MSC-loaded collagen hydrogels and ARSs that were subcutaneously implanted in mice. ADV was generated on day 1. B) ARSs appeared brighter than collagen-only constructs due to PSDE. ADV further increased the brightness on day 1 and day 3. C) Bubbles slowed down the compaction of the ARS compared to collagen-only constructs. N = 8–10 constructs per group in panels B and C. D) H&E-stained slides highlight the presence of bubbles within MSC-loaded ARSs. The implanted constructs were harvested 7 or 14 days after implantation. Higher magnification images are shown in the second and fourth columns. E) The height of the constructs was measured from H&E-stained slides. Bubble metrics of F) diameter, G) density, and H) area fraction were also measured from H&E-stained slides. Bubble density is the number of bubbles normalized by ARS area. Bubble area fraction is the area fraction of the bubbles normalized by ARS area. N = 4–5 constructs per group in panels E, G, and H. N = 201–397 bubbles per group in panel F. Significant differences are denoted as follows: *p < 0.05, **p < 0.01, ***p < 0.001, and ****p < 0.0001; ns denotes a non-significant difference.

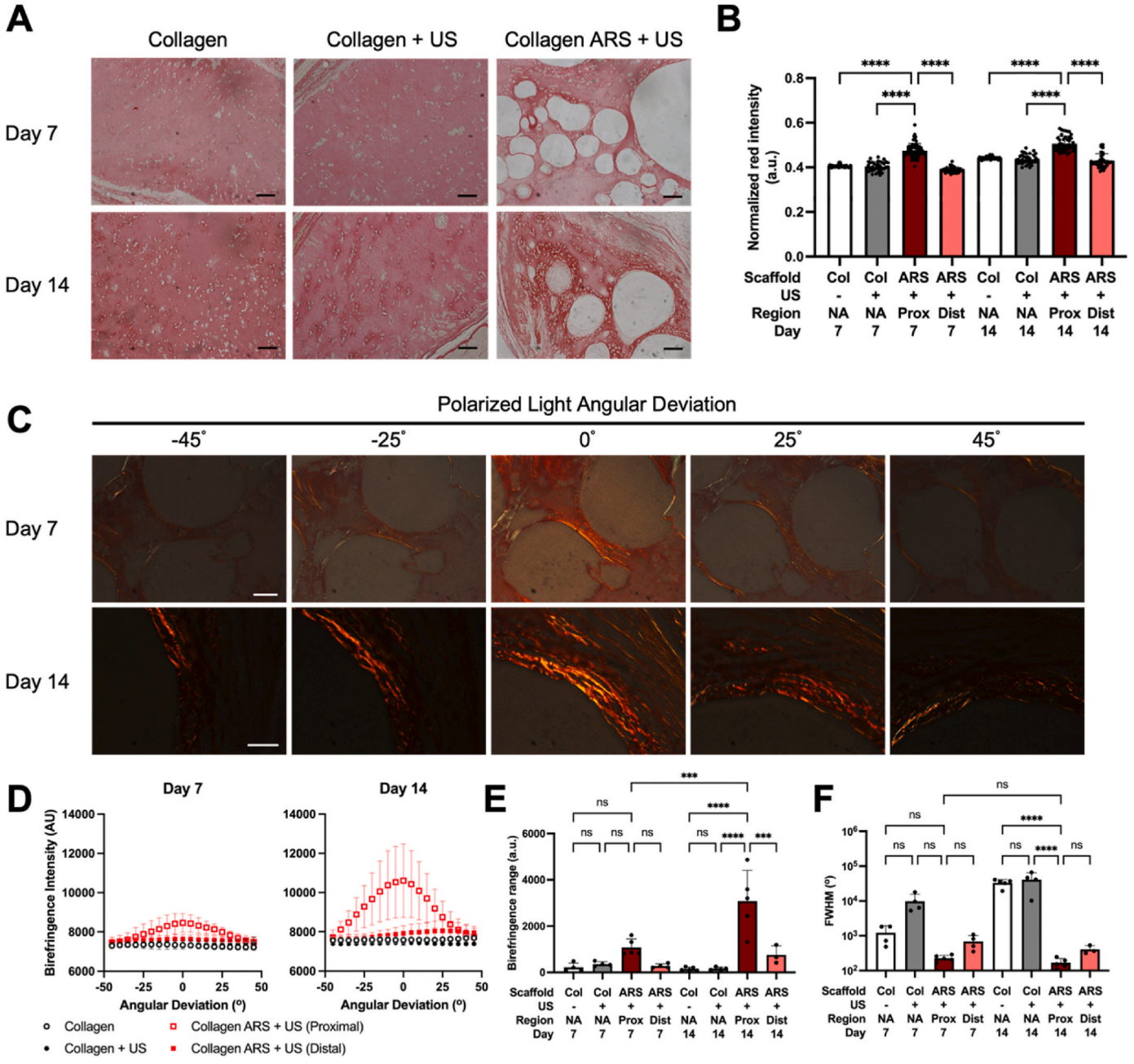

Fig. 7. ADV-generated bubbles led to alignment of collagen fibers. A) Brightfield images of Picrosirius red-stained sections of ARSs and collagen-only constructs explanted on day 7 and day 14. Scale bar = 100 μm. B) Normalized red intensity was quantified in proximal (prox) and distal (dist) regions of ARSs and collagen-only constructs (Col). C) Polarized light images of ARSs were taken over a range of angular deviation. Scale bar = 50 μm. D) Birefringence intensity is plotted as a function of angular deviation. The E) range of birefringence intensity and F) full width at half maximum (FWHM) were derived from data in panel D. Significant differences are denoted as follows: *p < 0.05, **p < 0.01, ***p < 0.001, and ****p < 0.0001; ns denotes a non-significant difference. N = 4–5 constructs per group.

3.8. In situ stiffening of ARSs in vivo upregulates osteogenic differentiation

We used non-invasive ultrasound to generate ADV within subcutaneously implanted ARSs containing MSCs, thereby enabling in situ stiffening. An ectopic model was used because the subcutaneous environment contains few osteoinductive factors and lacks naturally occurring bone-forming stem cells. Therefore, any observed differentiation toward bone cells could be attributed to the exogenous stem cells introduced. Immunohistochemical staining of RUNX2, OCN, and CD90 in ARSs explanted on day 7 and day 14 is shown (Fig. 8). Supplementary Fig. S5 displays images of collagen-only constructs.

On day 7, a significantly higher N/C ratio of RUNX2 was observed in the proximal (3.5 ± 1.7) versus distal region (3.3 ± 1.5) (Fig. 8A–C). Interestingly, nuclear translocation of RUNX2 remained significantly elevated in the proximal region (3.8 ± 1.5) on day 14 compared to the distal region (3.3 ± 1.5). The RUNX2 N/C ratio in collagen-only constructs is also shown (Fig. 8D). A significant increase in OCN expression was noted between proximal regions on day 14 versus day 7 (Fig. 8E–G). On day 14, OCN expression was higher in the proximal region compared to both the distal region and collagen-only gel (Fig. 8H), suggesting that ADV-based, matrix consolidation facilitated MSC commitment to osteoblasts. Moreover, CD90 expression was higher on day 7 compared to day 14 in both proximal and distal regions (Fig. 8I–L), indicating the maintenance of stem cell-like behavior of D1 MSCs by the end of the first week. The percent difference between groups and p-values for pairwise comparisons for RUNX2, OCN, and CD90 are found in Supplemental Fig. S6. The investigation also delved into the potential of encapsulated MSCs to differentiate into an adipogenic lineage, as assessed through the expression level of PPAR-γ (Supplemental Fig. S7). PPAR-γ, functioning as a transcription factor, regulates the expression of genes involved in cellular processes involved in adipogenic differentiation [53]. On day 7, the nuclear intensity of PPAR-γ expression was significantly higher in the distal region compared to the proximal region. By day 14, PPAR-γ levels decreased, with no significant difference between proximal and distal regions.

Explanted constructs were also evaluated for mineralization by staining with Alizarin red, whereby elevated staining was observed in the bubble region of the ARS (Fig. 9A). Quantification of the images revealed significantly greater staining in the proximal region of the ARS compared to the distal region as well as collagen-only constructs (Fig. 9B). Furthermore, we also evaluated blood vessel formation within the constructs due its importance for the survival of implanted cells (Supplemental Fig. S8). For all groups, vessel density and penetration distance increased from day 7 to day 14. However, no significant differences were observed between groups.

4. Discussion

Biomaterials research has traditionally focused on the development of materials with preprogrammed compositions and characteristics [54]. More recently, there has been a significant push towards developing biomaterials that can be externally controlled in a spatiotemporal manner [55]. This effort aims to replicate the dynamic microenvironments found in natural tissues, which are crucial for regulating cell behaviors and functions, as well as provide user-directed control of regenerative processes which intrinsically involve dynamic microenvironmental biochemical and biophysical cues. Given this objective, here we investigated the effect of ultrasound-mediated matrix compaction on the osteogenic differentiation of MSCs. The current study leveraged an innovative ARS technology previously developed by our group for on-demand drug delivery [42,56]. This is the first demonstration of using ADV to modulate matrix compaction to enhance MSC differentiation in 3D.

Consistent with previous studies in fibrin-based ARSs [41,57], ADV occurred at lower rarefactional pressures than IC in collagen-based ARSs. IC is the rapid growth and collapse of a bubble that is driven by the inertia of the surrounding medium. Stable bubbles were generated at 37°C following ADV of PSDE containing perfluorohexane, which has a bulk boiling point of ~56°C. The diffusion of dissolved gases from the surrounding microenvironment into the generated bubble [58] as well as the high solubility of oxygen within PFC liquids [59] assist with bubble stability. PFCs, especially those with longer carbon chain lengths like perfluorohexane, have coefficients of diffusivity, solubility, and permeability that are considerably lower than air (i.e., O_2, N_2, etc.) [60]. This, in addition to the large size of the ADV-generated bubbles that increases dissolution time [61], also contributes to bubble stability within the ARS. As seen in the in vivo data, there was bubble destabilization when comparing day 7 and day 14 that can be attributed to mechanisms like dissolution, Ostwald ripening, and coalescence [62].

The Young's modulus increased significantly in the matrix region proximal to the ADV-generated bubble due to compaction and was similar to the modulus of osteoid tissue [63]. However, the modulus in the proximal region did not increase over time, which is distinct from a prior study in fibrin-based ARSs [36]. One key difference is the initial modulus of the collagen-based ARS (4.2 kPa on day 1) was significantly higher than the fibrin-based ARS (0.5 kPa) in the distal region. Thus, the ability of ADV to locally increase stiffness appears to be dependent on both the initial modulus of the matrix and matrix composition. Here, the measured values reflect the micromechanical properties of collagen in the vicinity of ADV-generated bubbles and PSDEs. The hierarchical structure and orientation of collagen fibers (i.e., from individual triple helical molecules to assembled fibrils and larger fibers) play a crucial role in the anisotropic, mechanical properties of bone tissue [64,65]. Collagen fibers exhibit nonlinear elastic behavior, with stiffness increasing with strain (i.e., strain stiffening). This behavior is influenced by the entropic elasticity of the collagen molecules (entropic model) and the geometric alignment of fibers, contributing to the anisotropic mechanical response of bone. The entropic model also suggests that the elasticity of individual collagen fibers does not follow a simple, linear relationship with strain. Instead, their resistance to being stretched increases disproportionately as they are extended. The non-linear elasticity behavior of collagen fibers could explain the arrest in modulus increase of the proximal region over time [66,67].

MSCs respond to their physical microenvironment, including substrate stiffness, via mechanotransduction. We observed greater nuclear translocation of RUNX2 and higher expression of OCN in encapsulated MSCs located proximal ($\leq W_c$) versus distal ($>W_c$) to the bubble. This suggests that localized compaction and stiffening of the collagen matrix by ADV boosted the expression of bone markers, guiding encapsulated MSCs toward osteogenic differentiation. Previously, MSCs adhered to PEG hydrogels that were photostiffened from 1 kPa to 12 kPa (shear storage modulus) exhibited a 3-fold and 47% increase in RUNX2 mRNA expression and nuclear translocation, respectively, after 72 h [28]. However, in this study, N/C ratios decreased from day 7 to day 14. Prior studies have illustrated a dynamic pattern of RUNX2 expression during osteoblast differentiation [68,69]. During early stages, nuclear translocation of RUNX2 increases as MSCs commit to the osteoblast lineage and differentiate into preosteoblasts. As differentiation progresses, the expression of RUNX2 and its nuclear translocation may decrease slightly or remain relatively stable as other transcription factors and signaling pathways become activated to further promote osteoblast maturation and function [70]. Our in vivo results showed elevated N/C ratio of RUNX2 in the proximal region even on day 14. This suggests a slower or prolonged early osteogenic phase in the in vivo environment compared to in vitro culture. The duration of this commitment phase or the kinetics of osteogenic differentiation can be influenced by various factors such as culture conditions, growth factors, cell source, and mechanical stimuli [49,71]. In vitro experiments were conducted in bipotential media with growth factors, cytokines and other supplements that promoted differentiation; these external biochemical cues were absent in the in vivo studies.

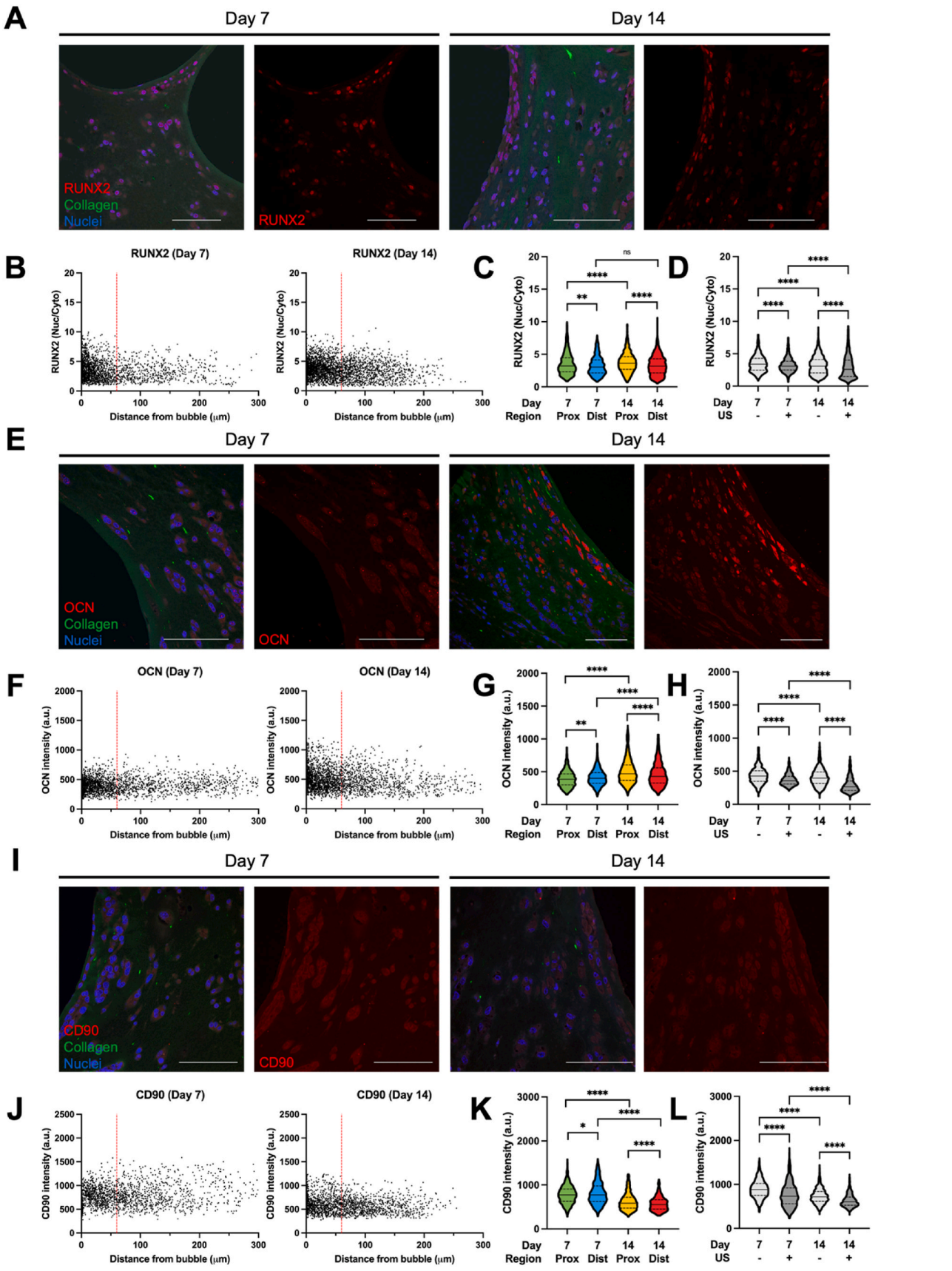

(caption on next page)

Fig. 8. Immunohistochemical analysis of in vivo differentiation of MSCs in collagen ARSs. A) Confocal micrographs show the nuclear localization of RUNX2 on day 7 and day 14. B) The N/C ratio of RUNX2 is plotted versus distance from the bubble-collagen interface. The dotted red line is W_c. The N/C ratio in C) ARSs and D) collagen-only gels on day 7 and day 14 is displayed. Proximal (prox) and distal (dist) regions are shown in panel C. N = 577–2408 cells per group. E) Confocal micrographs show the expression of OCN on day 7 and day 14. F) The intensity of OCN expression is plotted versus distance from the bubble-collagen interface. OCN intensity in G) ARSs and H) collagen-only gels. N = 884–1901 cells per group. I) Confocal micrographs show the expression of CD90 on day 7 and day 14. J) The intensity of CD90 expression is plotted versus distance from the bubble-collagen interface. CD90 intensity in K) ARSs and L) collagen-only gels. N = 858–1071 cells per group. Significant differences are denoted as follows: *p < 0.05, **p < 0.01, ***p < 0.001, and ****p < 0.0001; ns denotes a non-significant difference. All scale bars are 100 μm.

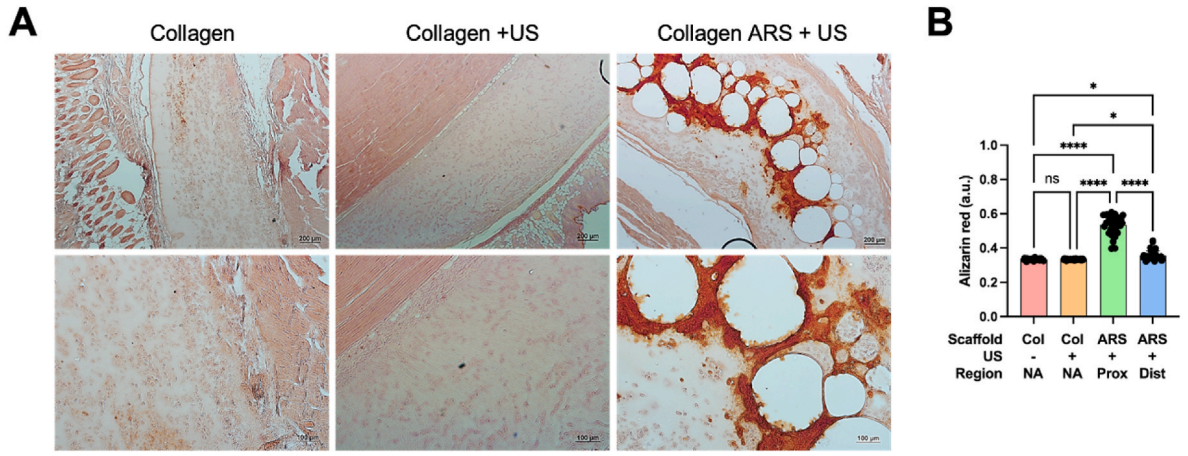

Fig. 9. ADV-generated bubbles enhanced in vivo mineralization. A) Elevated Alizarin red staining was observed in ARSs explanted on day 14. Higher magnification images are shown in the second row. Scale bars: 200 μm (top row) and 100 μm (bottom row). B) The intensity of Alizarin red staining is shown for each group. Significant differences are denoted as follows: *p < 0.05, and ****p < 0.0001; ns denotes a non-significant difference.

Investigating the adipogenic behavior of MSCs, the expression of PPAR-γ may be attributed to their pre-commitment stage and basal production level [72]. However, PPAR-γ expression in the proximal region was relatively low compared to the distal region suggesting a phenotypic shift of MSCs when in a stiffer matrix. By the end of two weeks, PPAR-γ expression decreased regardless of cell location, indicating the commitment of MSCs toward an osteogenic lineage.

Ultrasound, specifically low-intensity pulsed ultrasound (LIPUS), has been approved by the United States Food and Drug Administration to promote fracture healing [73]. Though LIPUS parameters (i.e., frequency, pressure, duty cycle) are very different than the ultrasound parameters used to generate ADV in this study, it is important to highlight relevant findings. LIPUS increased RUNX2 gene expression of MSCs in osteogenic media and decreased expression of PPAR-γ in adipogenic media [74]. Other studies have noted increases in RUNX2 and OCN expression in both growth and osteogenic media [75–77]. Our in vitro studies revealed that MSCs exposed to ultrasound within a collagen-only hydrogel exhibited no change in RUNX2 expression and a decrease in OCN levels (day 7 only) compared to a group without ultrasound.

As indicated by birefringence imaging, ADV-generated bubbles caused alignment of the collagen matrix in the proximal region, where greater nuclear elongation was also observed. Coupled with the collagen structure observed by confocal microscopy, it appears that collagen alignment was circumferential to the bubble-collagen interface. In the absence of ADV, minimal alignment was observed within the collagen matrix. Decreases in nuclear circularity have been associated with depletion of lamin A/C and markers of adipogenesis [78]. In general, topographical features of substrates and hydrogels have been shown to influence MSC behaviors. Osteogenic differentiation was enhanced when MSCs were cultured on aligned versus randomly oriented fibers [51]. Nuclear morphology of MSCs was also more sensitive to scaffold architecture than differentiated fibrochondrocytes [79].

For in situ, bone regeneration, implanted biomaterials should facilitate recruitment of MSCs and other relevant host cells [80]. However, conventional scaffolds used for bone regeneration often possess high stiffnesses and low porosities, which impede host cell invasion. The use of an ARS, potentially in combination with ultrasound-mediated cytokine delivery, could facilitate in situ regeneration by enabling on-demand control of matrix stiffening after endogenous MSC migration. One limitation of the presented technique is the spatial heterogeneity of bubbles within the ARS. A potential strategy to increase homogeneity is to spatially pattern emulsion and thus resulting ADV-induced bubbles using bioprinting [81]. Future research efforts will focus on assessing the impact of ultrasound and hydrogel parameters on ADV-mediated compaction. For example, maximizing the fraction of matrix compacted by ADV could be relevant. Additionally, the synergy of ADV to trigger release of bioactive factors, in addition to matrix compaction, could be beneficial in providing MSCs with relevant biochemical and biophysical cues required for differentiation.

5. Conclusions

Ultrasound was used to generate bubbles within composite collagen ARSs via the vaporization of perfluorohexane-loaded emulsion. Bubbles radially compacted the surrounding collagen matrix, which led to a significant increase in the Young's modulus proximal to the bubble. Bubble generation did not impact the viability or proliferation of MSCs encapsulated within the ARS. MSCs proximal to the bubble exhibited higher nuclear localization of RUNX2 with elevated levels OCN expression and decreased levels of CD90 compared to MSCs distal to the bubble. Bubbles also caused localized alignment of the collagen fibers that was associated with increased nuclear asymmetry. Overall, these results highlight the potential of using an ARS to non-invasively modulate MSC behaviors.

Ethics approval and consent to participate

All animal procedures were approved by the University of Michigan Institutional Animal Care and Use Committee. This study does not include human subjects.

CRediT authorship contribution statement

Somnath Maji: Writing – review & editing, Writing – original draft, Visualization, Methodology, Investigation, Formal analysis, Conceptualization. **Mitra Aliabouzar:** Writing – review & editing, Software, Methodology. **Carole Quesada:** Writing – review & editing, Methodology, Investigation. **Anjali Chiravuri:** Writing – review & editing, Investigation, Formal analysis. **Aidan Macpherson:** Writing – review & editing, Investigation, Formal analysis. **Abigail Pinch:** Formal analysis. **Karsyn Kazyak:** Formal analysis. **Ziyad Emara:** Writing – review & editing, Formal analysis. **Bachir A. Abeid:** Writing – review & editing, Methodology, Investigation. **Robert N. Kent:** Writing – review & editing, Software, Methodology. **Firaol S. Midekssa:** Writing – review & editing, Methodology. **Man Zhang:** Writing – review & editing, Conceptualization. **Brendon M. Baker:** Writing – review & editing, Resources, Methodology, Conceptualization. **Renny T. Franceschi:** Writing – review & editing, Resources, Methodology, Conceptualization. **Mario L. Fabiilli:** Writing – review & editing, Writing – original draft, Visualization, Supervision, Resources, Project administration, Methodology, Investigation, Funding acquisition, Formal analysis, Conceptualization.

Declaration of competing interest

The authors declare that they have no known competing financial interests or personal relationships that could have appeared to influence the work reported in this paper.

Acknowledgements

This work was supported by the Focused Ultrasound Foundation and NIH grant R01HL139656. The authors would like to thank Dr. Tanpreet Kaur and Dr. David Raffel for assisting with the synthesis of the fluorosurfactant. Additional thanks to Dr. Jon Estrada for letting us use his ultra-high-speed camera and high intensity pulsed laser.

Appendix A. Supplementary data

Supplementary data to this article can be found online at https://doi.org/10.1016/j.bioactmat.2024.09.018.

References

[1] D. Dey, B.M. Wheatley, D. Cholok, S. Agarwal, P.B. Yu, B. Levi, T.A. Davis, The traumatic bone: trauma-induced heterotopic ossification, Transl. Res. 186 (2017) 95–111.
[2] D.S. Chun, K.C. Baker, W.K. Hsu, Lumbar pseudarthrosis: a review of current diagnosis and treatment, Neurosurg. Focus 39 (4) (2015).
[3] P.I. Eke, B.A. Dye, L. Wei, G.O. Thornton-Evans, R.J. Genco, C.P.D. Surveillance, Prevalence of periodontitis in adults in the United States: 2009 and 2010, J. Dent. Res. 91 (10) (2012) 914–920.
[4] A. Oryan, S. Alidadi, Reconstruction of radial bone defect in rat by calcium silicate biomaterials, Life Sci. 201 (2018) 45–53.
[5] C.A. Pagani, A.C. Bancroft, R.J. Tower, N. Livingston, Y. Sun, J.Y. Hong, R. N. Kent 3rd, A.L. Strong, J.H. Nunez, J.M.R. Medrano, N. Patel, B.A. Nanes, K. M. Dean, Z. Li, C. Ge, B.M. Baker, A.W. James, S.J. Weiss, R.T. Franceschi, B. Levi, Discoidin domain receptor 2 regulates aberrant mesenchymal lineage cell fate and matrix organization, Sci. Adv. 8 (51) (2022) eabq6152.
[6] G.B.D.F. Collaborators, Global, regional, and national burden of bone fractures in 204 countries and territories, 1990-2019: a systematic analysis from the Global Burden of Disease Study 2019, Lancet Healthy Longev 2 (9) (2021) e580–e592.
[7] G.M. Raghoebar, R.S. Liem, R.R. Bos, J.E. van der Wal, A. Vissink, Resorbable screws for fixation of autologous bone grafts, Clin. Oral Implants Res. 17 (3) (2006) 288–293.
[8] A. Kinaci, V. Neuhaus, D.C. Ring, Trends in bone graft use in the United States, Orthopedics 37 (9) (2014).
[9] F. Shang, Y. Yu, S. Liu, L. Ming, Y. Zhang, Z. Zhou, J. Zhao, Y. Jin, Advancing application of mesenchymal stem cell-based bone tissue regeneration, Bioact. Mater. 6 (3) (2021) 666–683.
[10] Y. Liu, R. Yang, S. Shi, Systemic infusion of mesenchymal stem cells improves cell-based bone regeneration via upregulation of regulatory T cells, Tissue engineering, Part. Accel. 21 (3–4) (2015) 498–509.
[11] F.A. Probst, R. Fliefel, E. Burian, M. Probst, M. Eddicks, M. Cornelsen, C. Riedl, H. Seitz, A. Aszodi, M. Schieker, S. Otto, Bone regeneration of minipig mandibular defect by adipose derived mesenchymal stem cells seeded tri-calcium phosphate-poly(D,L-lactide-co-glycolide) scaffolds, Sci. Rep. 10 (1) (2020) 2062.
[12] Z.M. Johnson, Y. Yuan, X. Li, T. Jashashvili, M. Jamieson, M. Urata, Y. Chen, Y. Chai, Mesenchymal stem cells and three-dimensional-osteoconductive scaffold regenerate calvarial bone in critical size defects in swine, Stem Cells Transl Med 10 (8) (2021) 1170–1183.
[13] N. Cuende, J.E.J. Rasko, M.B.C. Koh, M. Dominici, L. Ikonomou, Cell, tissue and gene products with marketing authorization in 2018 worldwide, Cytotherapy 20 (11) (2018) 1401–1413.
[14] O. Levy, R. Kuai, E.M.J. Siren, D. Bhere, Y. Milton, N. Nissar, M. De Biasio, M. Heinelt, B. Reeve, R. Abdi, M. Alturki, M. Fallatah, A. Almalik, A.H. Alhasan, K. Shah, J.M. Karp, Shattering barriers toward clinically meaningful MSC therapies, Sci. Adv. 6 (30) (2020) eaba6884.
[15] J.A. Burdick, R.L. Mauck, S. Gerecht, To serve and protect: hydrogels to improve stem cell-based therapies, Cell Stem Cell 18 (1) (2016) 13–15.
[16] J. Li, Y. Liu, Y. Zhang, B. Yao, Enhejirigala, Z. Li, W. Song, Y. Wang, X. Duan, X. Yuan, X. Fu, S. Huang, Biophysical and biochemical cues of biomaterials guide mesenchymal stem cell behaviors, Front. Cell Dev. Biol. 9 (2021) 640388.
[17] A.S. Mao, J.W. Shin, D.J. Mooney, Effects of substrate stiffness and cell-cell contact on mesenchymal stem cell differentiation, Biomaterials 98 (2016) 184–191.
[18] B. Yi, Q. Xu, W. Liu, An overview of substrate stiffness guided cellular response and its applications in tissue regeneration, Bioact. Mater. 15 (2022) 82–102.
[19] O. Chaudhuri, L. Gu, D. Klumpers, M. Darnell, S.A. Bencherif, J.C. Weaver, N. Huebsch, H.-p. Lee, E. Lippens, G.N. Duda, D.J. Mooney, Hydrogels with tunable stress relaxation regulate stem cell fate and activity, Nat. Mater. 15 (3) (2016) 326.
[20] G. Abagnale, M. Steger, V.H. Nguyen, N. Hersch, A. Sechi, S. Joussen, B. Denecke, R. Merkel, B. Hoffmann, A. Dreser, U. Schnakenberg, A. Gillner, W. Wagner, Surface topography enhances differentiation of mesenchymal stem cells towards osteogenic and adipogenic lineages, Biomaterials 61 (2015) 316–326.
[21] W. Zhao, X. Li, X. Liu, N. Zhang, X. Wen, Effects of substrate stiffness on adipogenic and osteogenic differentiation of human mesenchymal stem cells, Mater. Sci. Eng., C 40 (2014) 316–323.
[22] H.I. Gungordu, M. Bao, S. van Helvert, J.A. Jansen, S.C.G. Leeuwenburgh, X. F. Walboomers, Effect of mechanical loading and substrate elasticity on the osteogenic and adipogenic differentiation of mesenchymal stem cells, Journal of tissue engineering and regenerative medicine 13 (12) (2019) 2279–2290.
[23] N. Huebsch, P.R. Arany, A.S. Mao, D. Shvartsman, O.A. Ali, S.A. Bencherif, J. Rivera-Feliciano, D.J. Mooney, Harnessing traction-mediated manipulation of the cell/matrix interface to control stem-cell fate, Nat. Mater. 9 (6) (2010) 518–526.
[24] X.T. He, R.X. Wu, X.Y. Xu, J. Wang, Y. Yin, F.M. Chen, Macrophage involvement affects matrix stiffness-related influences on cell osteogenesis under three-dimensional culture conditions, Acta Biomater. 71 (2018) 132–147.
[25] S.H. Parekh, K. Chatterjee, S. Lin-Gibson, N.M. Moore, M.T. Cicerone, M.F. Young, C.G. Simon, Modulus-driven differentiation of marrow stromal cells in 3D scaffolds that is independent of myosin-based cytoskeletal tension, Biomaterials 32 (9) (2011) 2256–2264.
[26] M.S. Ting, J. Travas-Sejdic, J. Malmstrom, Modulation of hydrogel stiffness by external stimuli: soft materials for mechanotransduction studies, J. Mater. Chem. B 9 (37) (2021) 7578–7596.
[27] Y. Shou, L. Liu, Q. Liu, Z. Le, K.L. Lee, H. Li, X. Li, D.Z. Koh, Y. Wang, T.M. Liu, Z. Yang, C.T. Lim, C. Cheung, A. Tay, Mechano-responsive hydrogel for direct stem cell manufacturing to therapy, Bioact. Mater. 24 (2023) 387–400.
[28] A.R. Killaars, C.J. Walker, K.S. Anseth, Nuclear mechanosensing controls MSC osteogenic potential through HDAC epigenetic remodeling, Proc. Natl. Acad. Sci. U.S.A. 117 (35) (2020) 21258–21266.
[29] A.M. Kloxin, M.W. Tibbitt, A.M. Kasko, J.A. Fairbairn, K.S. Anseth, Tunable hydrogels for external manipulation of cellular microenvironments through controlled photodegradation, Adv Mater 22 (1) (2010) 61.
[30] H.Y. Yoshikawa, F.F. Rossetti, S. Kaufmann, T. Kaindl, J. Madsen, U. Engel, A. L. Lewis, S.P. Armes, M. Tanaka, Quantitative evaluation of mechanosensing of cells on dynamically tunable hydrogels, J. Am. Chem. Soc. 133 (5) (2011) 1367–1374.
[31] A.A. Abdeen, J. Lee, N.A. Bharadwaj, R.H. Ewoldt, K.A. Kilian, Temporal modulation of stem cell activity using magnetoactive hydrogels, Adv. Healthcare Mater. 5 (19) (2016) 2536–2544.
[32] G. ter Haar, Therapeutic applications of ultrasound, Prog. Biophys. Mol. Biol. 93 (1–3) (2007) 111–129.
[33] M.L. Fabiilli, C.G. Wilson, F. Padilla, F.M. Martin-Saavedra, J.B. Fowlkes, R. T. Franceschi, Acoustic droplet-hydrogel composites for spatial and temporal control of growth factor delivery and scaffold stiffness, Acta Biomater. 9 (7) (2013) 7399–7409.
[34] O.D. Kripfgans, J.B. Fowlkes, D.L. Miller, O.P. Eldevik, P.L. Carson, Acoustic droplet vaporization for therapeutic and diagnostic applications, Ultrasound Med. Biol. 26 (7) (2000) 1177–1189.
[35] D.S. Li, O.D. Kripfgans, M.L. Fabiilli, J.B. Fowlkes, J.L. Bull, Initial nucleation site formation due to acoustic droplet vaporization, Appl. Phys. Lett. 104 (6) (2014).
[36] M. Aliabouzar, C.D. Davidson, W.Y. Wang, O.D. Kripfgans, R.T. Franceschi, A. J. Putnam, J.B. Fowlkes, B.M. Baker, M.L. Fabiilli, Spatiotemporal control of micromechanics and microstructure in acoustically-responsive scaffolds using acoustic droplet vaporization, Soft Matter 16 (28) (2020) 6501–6513.
[37] M. Aliabouzar, B.A. Abeid, O.D. Kripfgans, J.B. Fowlkes, J.B. Estrada, M.L. Fabiilli, Real-time spatiotemporal characterization of mechanics and sonoporation of

acoustic droplet vaporization in acoustically responsive scaffolds, Appl. Phys. Lett. 123 (11) (2023) 114101.
[38] A.S. Rowlands, P.A. George, J.J. Cooper-White, Directing osteogenic and myogenic differentiation of MSCs: interplay of stiffness and adhesive ligand presentation, Am. J. Physiol. Cell Physiol. 295 (4) (2008) C1037–C1044.
[39] M.E. Abdelgawad, K. Soe, T.L. Andersen, D.M. Merrild, P. Christiansen, P. Kjaersgaard-Andersen, J.M. Delaisse, Does collagen trigger the recruitment of osteoblasts into vacated bone resorption lacunae during bone remodeling? Bone 67 (2014) 181–188.
[40] M. Aliabouzar, X. Lu, O.D. Kripfgans, J.B. Fowlkes, M.L. Fabiilli, Acoustic droplet vaporization in acoustically-responsive scaffolds: effects of frequency of excitation, volume fraction, and threshold determination method, Ultrasound Med. Biol. 45 (12) (2019) 3246–3260.
[41] M. Aliabouzar, A. Jivani, X.F. Lu, O.D. Kripfgans, J.B. Fowlkes, M.L. Fabiilli, Standing wave-assisted acoustic droplet vaporization for single and dual payload release in acoustically-responsive scaffolds, Ultrason. Sonochem. 66 (2020).
[42] A. Moncion, M. Lin, E.G. O'Neill, R.T. Franceschi, O.D. Kripfgans, A.J. Putnam, M. L. Fabiilli, Controlled release of basic fibroblast growth factor for angiogenesis using acoustically-responsive scaffolds, Biomaterials 140 (2017) 26–36.
[43] B.A. Abeid, M.L. Fabiilli, J.B. Estrada, M. Aliabouzar, Ultra-high-speed dynamics of acoustic droplet vaporization in soft biomaterials: effects of viscoelasticity, frequency, and bulk boiling point, Ultrason. Sonochem. 103 (2024) 106754.
[44] B. Das, P. Chattopadhyay, D. Mishra, T.K. Maiti, S. Maji, R. Narayan, N. Karak, Nanocomposites of bio-based hyperbranched polyurethane/funtionalized MWCNT as non-immunogenic, osteoconductive, biodegradable and biocompatible scaffolds in bone tissue engineering, J. Mater. Chem. B 1 (33) (2013) 4115–4126.
[45] Z. Liu, X. Yao, G. Yan, Y. Xu, J. Yan, W. Zou, G. Wang, Mediator MED23 cooperates with RUNX2 to drive osteoblast differentiation and bone development, Nat. Commun. 7 (2016) 11149.
[46] R.T. Franceschi, G. Xiao, Regulation of the osteoblast-specific transcription factor, Runx2: responsiveness to multiple signal transduction pathways, J. Cell. Biochem. 88 (3) (2003) 446–454.
[47] M.L. Zoch, T.L. Clemens, R.C. Riddle, New insights into the biology of osteocalcin, Bone 82 (2016) 42–49.
[48] M. Ponzetti, N. Rucci, Osteoblast differentiation and signaling: established Concepts and emerging topics, Int. J. Mol. Sci. 22 (13) (2021).
[49] H.C. Blair, Q.C. Larrouture, Y. Li, H. Lin, D. Beer-Stoltz, L. Liu, R.S. Tuan, L. J. Robinson, P.H. Schlesinger, D.J. Nelson, Osteoblast differentiation and bone matrix formation in vivo and in vitro, Tissue Eng., Part B 23 (3) (2017) 268–280.
[50] M. Dominici, K. Le Blanc, I. Mueller, I. Slaper-Cortenbach, F. Marini, D. Krause, R. Deans, A. Keating, D. Prockop, E. Horwitz, Minimal criteria for defining multipotent mesenchymal stromal cells. The International Society for Cellular Therapy position statement, Cytotherapy 8 (4) (2006) 315–317.
[51] H. Chen, Y. Qian, Y. Xia, G. Chen, Y. Dai, N. Li, F. Zhang, N. Gu, Enhanced osteogenesis of ADSCs by the synergistic effect of aligned fibers containing collagen I, ACS Appl. Mater. Interfaces 8 (43) (2016) 29289–29297.
[52] L. Rittie, Method for picrosirius red-polarization detection of collagen fibers in tissue sections, Methods Mol. Biol. 1627 (2017) 395–407.
[53] B.B. Lowell, PPARgamma: an essential regulator of adipogenesis and modulator of fat cell function, Cell 99 (3) (1999) 239–242.
[54] M.P. Lutolf, J.A. Hubbell, Synthetic biomaterials as instructive extracellular microenvironments for morphogenesis in tissue engineering, Nat. Biotechnol. 23 (1) (2005) 47–55.
[55] J. Leijten, J. Seo, K. Yue, G.T. Santiago, A. Tamayol, G.U. Ruiz-Esparza, S.R. Shin, R. Sharifi, I. Noshadi, M.M. Alvarez, Y.S. Zhang, A. Khademhosseini, Spatially and temporally controlled hydrogels for tissue engineering, Mater. Sci. Eng. R Rep. 119 (2017) 1–35.
[56] H. Jin, C. Quesada, M. Aliabouzar, O.D. Kripfgans, R.T. Franceschi, J.H. Liu, A. J. Putnam, M.L. Fabiilli, Release of basic fibroblast growth factor from acoustically-responsive scaffolds promotes therapeutic angiogenesis in the hind limb ischemia model, J. Contr. Release 338 (2021) 773–783.
[57] A. Moncion, K.J. Arlotta, O.D. Kripfgans, J.B. Fowlkes, P.L. Carson, A.J. Putnam, R. T. Franceschi, M.L. Fabiilli, Design and characterization of fibrin-based acoustically responsive scaffolds for tissue engineering applications, Ultrasound Med. Biol. 42 (1) (2016) 257–271.
[58] A.S. Hannah, G.P. Luke, S.Y. Emelianov, Blinking phase-change nanocapsules enable background-free ultrasound imaging, Theranostics 6 (11) (2016) 1866–1876.
[59] A.M.A. Dias, M. Freire, J.A.P. Coutinho, I.M. Marrucho, Solubility of oxygen in liquid perfluorocarbons, Fluid Phase Equil. 222 (2004) 325–330.
[60] A. Kabalnov, D. Klein, T. Pelura, E. Schutt, J. Weers, Dissolution of multicomponent microbubbles in the bloodstream: 1. Theory, Ultrasound Med. Biol. 24 (5) (1998) 739–749.
[61] K. Sarkar, A. Katiyar, P. Jain, Growth and dissolution of an encapsulated contrast microbubble: effects of encapsulation permeability, Ultrasound Med. Biol. 35 (8) (2009) 1385–1396.
[62] E. Talu, M.M. Lozano, R.L. Powell, P.A. Dayton, M.L. Longo, Long-term stability by lipid coating monodisperse microbubbles formed by a flow-focusing device, Langmuir 22 (23) (2006) 9487–9490.
[63] Y. Sugawara, R. Ando, H. Kamioka, Y. Ishihara, S.A. Murshid, K. Hashimoto, N. Kataoka, K. Tsujioka, F. Kajiya, T. Yamashiro, T. Takano-Yamamoto, The alteration of a mechanical property of bone cells during the process of changing from osteoblasts to osteocytes, Bone 43 (1) (2008) 19–24.
[64] M.P. Wenger, L. Bozec, M.A. Horton, P. Mesquida, Mechanical properties of collagen fibrils, Biophys. J. 93 (4) (2007) 1255–1263.
[65] P. Fratzl, K. Misof, I. Zizak, G. Rapp, H. Amenitsch, S. Bernstorff, Fibrillar structure and mechanical properties of collagen, J. Struct. Biol. 122 (1–2) (1998) 119–122.
[66] S. Nam, K.H. Hu, M.J. Butte, O. Chaudhuri, Strain-enhanced stress relaxation impacts nonlinear elasticity in collagen gels, Proc. Natl. Acad. Sci. U.S.A. 113 (20) (2016) 5492–5497.
[67] C. Storm, J.J. Pastore, F.C. MacKintosh, T.C. Lubensky, P.A. Janmey, Nonlinear elasticity in biological gels, Nature 435 (7039) (2005) 191–194.
[68] L. Song, N.E. Webb, Y. Song, R.S. Tuan, Identification and functional analysis of candidate genes regulating mesenchymal stem cell self-renewal and multipotency, Stem Cell. 24 (7) (2006) 1707–1718.
[69] C. Loebel, E.M. Czekanska, M. Bruderer, G. Salzmann, M. Alini, M.J. Stoddart, Osteogenic potential of human mesenchymal stem cells is predicted by runx2/sox9 ratio, Tissue Eng. 21 (1–2) (2015) 115–123.
[70] T. Komori, Regulation of proliferation, differentiation and functions of osteoblasts by Runx2, Int. J. Mol. Sci. 20 (7) (2019).
[71] L. Malaval, F. Liu, P. Roche, J.E. Aubin, Kinetics of osteoprogenitor proliferation and osteoblast differentiation in vitro, J. Cell. Biochem. 74 (4) (1999) 616–627.
[72] I. Takada, A.P. Kouzmenko, S. Kato, PPAR-Γ signaling crosstalk in mesenchymal stem cells, PPAR Res. 2010 (2010).
[73] R. Puts, R. Vico, N. Beilfuss, M. Shaka, F. Padilla, K. Raum, Pulsed ultrasound for bone regeneration - outcomes and hurdles in the clinical application: a systematic review, Eur. Cell. Mater. 42 (2021) 281–311.
[74] J. Kusuyama, K. Bandow, M. Shamoto, K. Kakimoto, T. Ohnishi, T. Matsuguchi, Low intensity pulsed ultrasound (LIPUS) influences the multilineage differentiation of mesenchymal stem and progenitor cell lines through ROCK-cot/tpl2-MEK-ERK signaling pathway, J. Biol. Chem. 289 (15) (2014) 10330–10344.
[75] C.Y. Chiu, T.L. Tsai, R. Vanderby, G. Bradica, S.L. Lou, W.J. Li, Osteoblastogenesis of mesenchymal stem cells in 3-D culture enhanced by low-intensity pulsed ultrasound through soluble receptor activator of nuclear factor kappa B ligand, Ultrasound Med. Biol. 41 (7) (2015) 1842–1852.
[76] V. Costa, V. Carina, S. Fontana, A. De Luca, F. Monteleone, S. Pagani, M. Sartori, S. Setti, C. Faldini, R. Alessandro, M. Fini, G. Giavaresi, Osteogenic commitment and differentiation of human mesenchymal stem cells by low-intensity pulsed ultrasound stimulation, J. Cell. Physiol. 233 (2) (2018) 1558–1573.
[77] Y. An, Y. Song, Z. Wang, J. Wang, G. Wu, G. Zhu, L. Chen, Effect of low-intensity pulsed ultrasound on the biological behaviors of bone marrow mesenchymal stem cells on titanium with different surface topographies, Am J Transl Res 10 (1) (2018) 67–76.
[78] M. Goelzer, A. Dudakovic, M. Olcum, B. Sen, E. Ozcivici, J. Rubin, A.J. van Wijnen, G. Uzer, Lamin A/C is dispensable to mechanical repression of adipogenesis, Int. J. Mol. Sci. 22 (12) (2021).
[79] A.S. Nathan, B.M. Baker, N.L. Nerurkar, R.L. Mauck, Mechano-topographic modulation of stem cell nuclear shape on nanofibrous scaffolds, Acta Biomater. 7 (1) (2011) 57–66.
[80] M. Herrmann, S. Verrier, M. Alini, Strategies to stimulate mobilization and homing of endogenous stem and progenitor cells for bone tissue repair, Front. Bioeng. Biotechnol. 3 (2015) 79.
[81] M. Aliabouzar, A.W.Y. Ley, S. Meurs, A.J. Putnam, B.M. Baker, O.D. Kripfgans, J. B. Fowlkes, M.L. Fabiilli, Micropatterning of acoustic droplet vaporization in acoustically-responsive scaffolds using extrusion-based bioprinting, Bioprinting 25 (e00188) (2022).